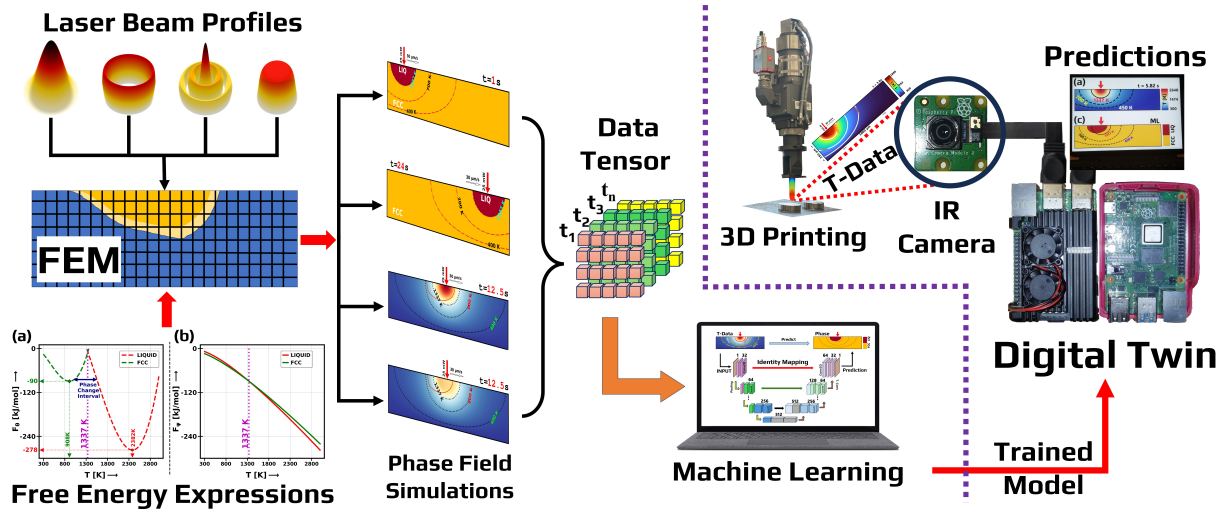


# Graphical Abstract

**A robust phase-field U-net framework to digitally identify the melt pools from different heat source models in real time.**

Upadesh Subedi, Nele Moelans, Tomasz Tański, Anil Kunwar



## Highlights

**A robust phase-field U-net framework to digitally identify the melt pools from different heat source models in real time.**

Upadesh Subedi, Nele Moelans, Tomasz Tański, Anil Kunwar

- Phase field modelling of Laser heat source types
- Virtual DT deployable as physical DT
- 
- 
- 
- Digital Twin

# A robust phase-field U-net framework to digitally identify the melt pools from different heat source models in real time.

Upadesh Subedi<sup>a,\*</sup>, Nele Moelans<sup>b</sup>, Tomasz Tański<sup>a</sup> and Anil Kunwar<sup>a</sup>

<sup>a</sup>Faculty of Mechanical Engineering, Silesian University of Technology, Konarskiego 18A, Gliwice, 44-100, Poland

<sup>b</sup>Department of Materials Engineering, KU Leuven, Kasteelpark Arenberg 44 Bus 2450, Leuven, 3001, Belgium

## ARTICLE INFO

### Keywords:

Moving Heat Source  
Super Gaussian Order  
Free Energy  
Precision Manufacturing  
Virtual Digital Twin  
Physics Informed VDT

## ABSTRACT

The uncertainties in the interaction between laser and microstructural interfaces pose a major hindrance to precision engineering in additive manufacturing. Proper assessment of the role of laser heat source types on microstructure evolution and phase transitions is crucial for understanding the process-property relationship of 3D-printed parts. To address this, we present a multimodal computational study that deciphers key aspects of thermal distribution, phase transformation, and the dynamics of thermal-to-phase diffusion fronts across different laser beam profiles and free energy expressions for an unary Au system. A detailed comparison of the microstructural pathways developed under four laser beam shapes—Gaussian, Flat-Top, Ring, and Bessel—and two different mathematical expressions for free energy was conducted. Furthermore, a U-Net machine learning model was trained on the simulation data to correlate temperature distribution with melt pool phase evolution, achieving training, validation, and test accuracies of 0.9992, 0.9989, and 0.9988, respectively. Additionally, we developed an interactive framework based on the trained model that can predict phase evolution from a user-supplied temperature distribution array. This framework provides a foundation for future work in constructing a Digital Twin model capable of real-time phase evolution prediction in experimental setups.

**Title: Machine Learning the Lewis number to obtain the phase information from thermal history just in time.**

## 1. Introduction

In today's world, product development is driven by speed, precision, and portability [1]. From medical devices to space technology, equipment and devices are designed to be increasingly agile, with frequent design updates [2, 3, 4]. To keep pace with advancements in materials, product dimensions, and quality, the manufacturing industry is increasingly adopting additive manufacturing. Within this framework, the role of heat deposition in metal additive manufacturing is critical, and accurate quantification of laser-material interactions is essential for ensuring reliable final products [5, 6].

This study presents a comprehensive computational analysis of how four distinct laser beam profiles affect microstructure evolution in a unary Au system. Phase-field simulations are used to capture the evolution of melt pool geometry, area, and thermal history within the computational domain. Additionally, we compare results from two approaches to free energy functionals in phase-field modeling: one based on expressions directly extracted from a Thermodynamic Database (TDB) file and another using a

fine-tuned, higher-order polynomial-logarithmic fitted function. Comparisons of free energy expressions in phase-field modeling are rare [7], as exact thermodynamic expressions are difficult to obtain, leading most studies to rely on polynomial fits derived from software like Thermo-Calc [8]. Moreover, such studies are often limited to free energy expressions at only two fixed temperatures for two phases [9]. This work distinguishes itself by integrating thermodynamic expressions for temperature-dependent free energies directly from a TDB file into a Finite Element Analysis (FEA) toolkit, as opposed to using fitted expressions at constant temperatures.

Modeling an additive manufacturing process, which involves multiple simultaneous physical processes, requires tightly coupled multi-physics simulations. In this study, the FEA simulation of laser heat treatment of a pure gold film undergoing phase transformation is conducted using MOOSE [10, 11], an open-source FEA toolkit. This simulation captures three key phenomena—laser heat deposition, phase-field modeling, and fluid flow within the melt pool—each fully coupled with the others.

In the literature, thermal diffusion and phase diffusion during laser heat treatment are often assumed to be identical, leading to the presumption that the liquid phase (melt pool) forms instantaneously when a region within the domain reaches a temperature above the material's melting point. This assumption overlooks the actual physical behavior in laser-based additive manufacturing processes, where phase diffusion lags behind thermal diffusion in the system [12]. In our study, we address this discrepancy by directly implementing the free energy functional from TDB files into the simulation toolkit. Results from the TDB-based free energy expression indicate a lead-lag behavior between thermal

 upadesh.subedi@polsl.pl (U. Subedi)

 <https://www.researchgate.net/profile/Upadesh-Subedi> (U. Subedi)

ORCID(s): 0000-0002-5527-1348 (U. Subedi); 0000-0003-3361-2954 (N. Moelans); 0000-0003-4024-1231 (T. Tański); 0000-0003-4295-5772 (A. Kunwar)

 <https://www.linkedin.com/profile/view?id=upadesh-s-0b321a15b> (U. Subedi)

and phase diffusion, which alters the melt pool geometry. This study establishes a clear distinction in modeling phase evolution during laser treatment by using both fine-tuned (fitted) free energy expressions and direct TDB expressions in phase-field simulations. The primary reason contemporary researchers often overlook the distinction between thermal and phase diffusion is computational efficiency. By assuming that the computational zone within the melting point temperature is equivalent to the liquid (melt pool) phase, and neglecting the differences between heat and mass diffusion, simulations can converge more quickly. However, this approach fails to capture the intricate interplay between thermal and phase diffusion, which affects other physical phenomena such as fluid flow, thermal conductivity, and density. To address the computational cost while preserving the accuracy of physical properties and phenomena within the computational domain, this work employs a machine learning (ML) approach to predict phase evolution based solely on temperature distribution, effectively incorporating the lead-lag dynamics of phase and thermal diffusion. The ML model is trained on a dataset generated through multi-physics phase-field simulations using a U-Net architecture [13].

In the following section, we discuss in detail the types of laser heat sources, their formulations, visualizations, and the expressions for thermodynamic driving forces considered in the phase-field simulation. We also explain the temperature-dependent material properties for the material under study and the machine learning architecture. In the Results and Discussion Section 8, we examine the effects on phase evolution, temperature distribution, and melt pool flow characteristics under different laser heat source applications, varying beam profiles, and distinct expressions of the free energy functional for phase-field modeling. To compare the different laser beam profiles, we keep the laser power (P), scan speed (v), and beam outer radius ( $r_x$ ) constant across all simulations.

#### Physics Informed Virtual Digital Twin

## 2. Initial and Boundary Conditions

In a unary system of pure Au undergoing laser heat treatment, a simulation domain of dimensions  $1000 \mu\text{m} \times 250 \mu\text{m}$  in the x-z direction is studied, as shown in Figure 1. The system consists of two phases: the LIQUID phase, representing molten gold, and the FCC phase, representing solid gold. Initially, at time ' $t_0$ ', a laser beam with a power of 25 mW is irradiated on the top surface at a distance of  $125 \mu\text{m}$  from the left, with a scan speed of  $30 \mu\text{m/s}$ , inducing a melt pool with an area of  $2500 \mu\text{m}^2$ . The computational domain is surrounded by an ambient environment at a temperature  $T_{air} = 300 \text{ K}$  on three sides (left, right, and top), while it rests on an interface with a heat transfer coefficient  $h_{int} = 11500 \text{ W/m}^2\text{K}$  [14]. The convective heat transfer coefficient of the air surrounding the domain is taken as  $h_{amb} = 50 \text{ W/m}^2\text{K}$  [15]. The non-isothermal process of laser heat deposition requires that the material properties of the system

be accurately represented as functions of temperature. These temperature-dependent properties, such as density, specific heat, and thermal conductivity, are discussed further in Section 6.

## 3. Non-isothermal phase field model for laser processing of Gold

The phase field model consists of two phases: the melt pool (LIQUID) and solid (FCC), which are represented by the non-conserved order parameter ' $\eta$ ' and ' $1 - \eta$ ' respectively. The value of ' $\eta$ ' is set to 1 inside the LIQUID phase and 0 in the FCC phase. Since this work follows the evolution of phases in a single-component system, the conserved variable 'composition' remains constant throughout the domain. Thus, this study focuses on the evolution of the two phases and the transformation induced by laser heat deposition. In this two-phase system, undergoing temperature variation at different spatial coordinates, a swift transition of material properties and their associated characteristics between the respective phases is required, and this transition must be thermodynamically consistent. To achieve this, we use the function  $h_i(\eta)$  provided by Moelans [16], as presented in Equation 1 [17] [18] unpublished.

$$h_i = \frac{\eta_i^2}{\sum_{k=1}^N \eta_k^2} \quad (1)$$

In the equation above, N represents the total number of order parameters in the system, with ' $i$ ' denoting a specific phase. The driving force dictating the morphological changes in the microstructure within the computational domain is the total free energy of the system. With an external heat source acting on the system, the total free energy ( $F_{total}$ ) can be modeled as the combination of bulk free energy ( $F_{bulk}$ ) and interfacial free energy ( $F_{int}$ ), as given by Equation 2.

$$F_{total} = F_{bulk} + F_{int} = \int_V (f_{bulk} + f_{int}) dV \quad (2)$$

here, the bulk and interfacial energies are expressed in terms of free energy densities (energy per unit molar volume of Au). The bulk free energy density ( $f_{bulk}$ ) and interfacial free energy density ( $f_{int}$ ) are further expressed in Equations 3 and 4 respectively.

$$f_{bulk} = \sum_i h_i f_{bulk}^i = \sum_i \frac{F_i(T)}{V_m} \quad (3)$$

In the above equation,  $h_i$  represents the interpolation function, whereas  $f_{bulk}^i$  denotes the bulk free energy density of the  $i^{th}$  phase.  $V_m$  is the molar volume of gold, with a value of  $10.21 \text{ cm}^3/\text{mol}$  [19], taken for both phases. Additionally,  $F_i(T)$  represents the temperature-dependent Gibbs

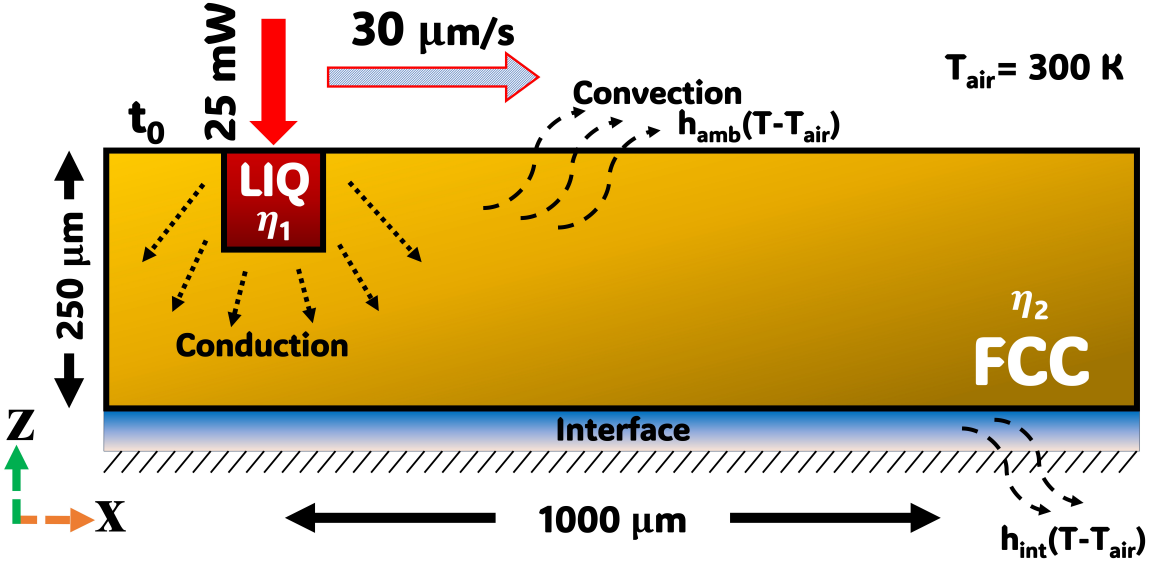


**Figure 1:** The schematic diagram of the computational domain setup illustrates the laser-induced phase evolution in Phase Field Modeling at time  $t_0$ . A  $1000 \mu\text{m} \times 250 \mu\text{m}$  section of a unary Au system in the  $x$ - $z$  coordinate system represents the simulation's length scale. The computational system rests on an interface at the bottom, with ambient air surrounding it on the other three sides. Heat transfer into the system occurs through conduction, while convective heat transfer occurs out of the system through the air and interface, as shown in the figure. A laser heat source with a power of  $25 \text{ mW}$  is irradiated on the top surface of the domain, positioned  $125 \mu\text{m}$  from the top-left corner, with a scan speed of  $30 \mu\text{m/s}$ , indicated by the red arrow just above the LIQUID phase. The initial LIQUID phase area, denoted by ' $\eta_1$ ' and representing the melt pool, is  $2500 \mu\text{m}^2$ , shown as a red-colored block, while the solid gold region is represented by the FCC phase, denoted by ' $\eta_2$ ' in the yellow-colored remaining area. The computational domain, phase structure, and initial areas, along with the laser processing parameters (power and scan speed), are kept identical across multiple simulations involving different laser beam profiles.

free energy of phase  $i$ . The free energy expressions, their formulation, and the graph of free energy versus temperature for the two phases are presented in detail in Section 4.

$$f_{int} = mf_{barrier} + \frac{\kappa}{2} \sum_i (\nabla \eta_i)^2 \quad (4)$$

where,  $m$  and  $\kappa$  are the model parameters associated with interfacial energy ( $\sigma [\text{J/m}^2]$ ) and diffused interface width ( $\delta [\text{m}]$ ) as follows:

$$m = \frac{6\sigma}{\delta} \quad (5)$$

$$\kappa = \frac{3}{4}\delta\sigma \quad (6)$$

In this study, we have set the value of the interface width  $\delta$  to be  $10 \mu\text{m}$  and the interfacial energy to  $0.5 \text{ J/m}^2$ . The term  $f_{barrier}$  in Equation 4 is a fourth-order Landau polynomial of the phase field variable, expressed as follows:

$$f_{barrier} = \sum_i \left( \frac{(\eta_i)^4}{4} - \frac{(\eta_i)^2}{2} \right) + \gamma \sum_i \sum_{j \neq i} \eta_i^2 \eta_j^2 + \frac{1}{4} \quad (7)$$

During laser processing, the spatio-temporal tracking of the non-conserved phase field variable 'order parameter' ( $\eta$ ) provides an accurate description of phase transformation. Equation 8 describes the evolution of the order parameter as follows:

$$\frac{\partial \eta_i}{\partial t} = -L(\eta_1, \dots, \eta_N) \left( \frac{\partial f_{bulk}}{\partial \eta_i} - \nabla \cdot \frac{\partial f_{int}}{\partial \nabla \eta_i} \right) \quad (8)$$

where,  $L(\eta_1, \dots, \eta_N) = L^i$  which is defined as follows:

$$L^i = \frac{\sum_{i=1}^N \sum_{j>1}^N L_{ij} \eta_i^2 \eta_j^2}{\sum_{i=1}^N \sum_{j>1}^N \eta_i^2 \eta_j^2} \quad (9)$$

The interfacial mobility in Equation 9 is further approximated as follows:

$$L_{ij} = \frac{4m}{3\kappa} \times \frac{M^i + M^j}{2} \quad (10)$$

here,  $M^i$  and  $M^j$  are the phase mobilities of the two adjacent phases, namely the LIQUID and FCC phases. Similarly, for the heat deposited by the laser source at the top

$$F_\theta = T_{th} \left[ A_\theta - B_\theta - C_\theta(T-T_0) + D_\theta(T-T_0) \ln(E_\theta T) + F_\theta(T-T_0)^2 + G_\theta(T-T_0)^3 + H_\theta T^{-1} \right]$$

$$F_\psi = \begin{cases} LIQUID & : A_\psi T \ln \left[ 1 - \exp(-B_\psi T^{-1}) \right] - RT \ln \left[ 1 + \exp \left( C_\psi (D_\psi - E_\psi T) T^{-1} \right) \right] - F_\psi T^2 - G_\psi \\ FCC & : A_\psi T \ln \left( 1 - \exp(-B_\psi T^{-1}) \right) - C_\psi + \begin{cases} T < 1337.33 & : D_\psi T^2 - E_\psi T^3 \\ T \geq 1337.33 & : F_\psi T^{-11} - G_\psi T^{-5} - H_\psi T \ln(T) + I_\psi T + J_\psi \end{cases} \end{cases}$$
(12)

surface of the computational domain, heat transfer follows the partial differential equation presented in Equation 11.

$$\rho^i C p^i \left( \frac{\partial T}{\partial t} + \vec{u} \cdot \nabla T \right) = k_{th}^i \nabla^2 T + Q_{laser} \quad (11)$$

In the above equation, temperature is denoted by  $T$  at time  $t$ . The density, specific heat capacity, and thermal conductivity of phase ‘ $i$ ’ are represented by  $\rho^i$ ,  $Cp^i$ , and  $k_{th}^i$ , respectively. The flow velocity inside the melt pool is given by  $\vec{u}$ , which contributes to convective heat transfer, while the external laser heat source is denoted by  $Q_{laser}$ . Since third of our study focuses on comparing the effects of different laser beam profiles, detailed descriptions of the external laser heat sources, their individual mathematical expressions, and 2D and 3D visualizations are provided in Section 5.

#### 4. Thermodynamic Driving Force

For computational efficiency and faster convergence, polynomial expressions of free energy are considered favorable, especially the parabolic expressions of second-order polynomials, which are frequently implemented for modeling binary [20] and ternary [21, 22] alloy systems. For binary, ternary, and multicomponent alloys, polynomial expressions with  $n > 2$  generally offer more accurate descriptions but are computationally expensive due to the compositional complexities that arise in the diffusion equations. In the laser heating of pure metals at constant pressure, the free energy is solely a function of temperature ( $T$ ) and not of composition. This allows for the flexibility to expand the polynomial expression beyond traditional parabolic forms and even to include logarithmic terms. Thus, the fitting expression for pure Au metal undergoing temperature change can be best described by the expression  $F_\theta$ , as presented in Equation 12, derived similarly to that of [23, 24]. This free energy expression is a differentially continuous function for a given phase, thereby ensuring numerical efficiency. In contrast, the TDB-based expressions ( $F_\psi$ ) are piecewise continuous functions of temperature even for a given phase, as shown in Equation 12, extracted from the Thermodynamic Data Base file formulated by Khvan et al. [25]. In this regard, many engineering applications: such as the development of Digital Twins may require the use of fitted expressions when computational efficiency is the primary concern.

In Equation 12, the coefficients  $A$ ,  $B$ ,  $C$ ,  $D$ ,  $E$ ,  $F$ ,  $G$ ,  $H$ ,  $I$ ,  $J$  and  $T_{th}$ , with subscripts ‘ $\theta$ ’ and ‘ $\psi$ ’, represent the thermodynamic coefficients of the free energy functional

for the fine-tuned and TDB-based expressions. The values of these coefficients are presented in Table 1 for both the LIQUID and FCC phases. In this equation, the temperature dependence of the free energy functional is depicted by the variable ‘ $T$ ’, which represents the temperature.

The two presented free-energy expressions are used with multiple laser beam profiles in laser-aided phase-field simulations. The effects of the free energy expressions—one based on a fine-tuned higher-order polynomial-logarithmic function and the other extracted directly from a thermodynamic data file, are analyzed through multiple simulations while keeping the other laser parameters fixed. The free energy expressions, along with their plots with respect to temperature and phase, are presented in Equation 12 and Figure 2, respectively. As observed in Figure 2, the  $F_\theta$  curves for the FCC and LIQUID phases are characterized by a distinct phase change interval, whereas the curves of  $F_\psi$  for the two phases, based on the as-obtained expressions lack this feature.

The benefits of using a fine-tuned (fitted) free energy expression are twofold: firstly, the expression is a fitted continuous and differentiable function across the entire temperature range, which is a key prerequisite for performing phase field simulations. Secondly, the fine-tuned function can be readily developed even with fewer energy-temperature data points, which is particularly useful for constructing digital twin models with new materials or elements. In Figure 2(a), the 2D plot of the fitted free energy versus temperature profile suggests the presence of an interval between two phases (LIQUID and FCC) near the melting temperature of gold (1337 K). This interval, known as the Phase Change Interval, dictates the rate of information relay of thermal history to phase evolution, where the interpolation function acts based on the specific phase at a given spatial location within the domain. A sharp or smaller phase change interval, such as in the case of pure metals, causes the phase transition to occur rapidly, often during the melting and solidification processes, which can create residual stresses [26, 27], along with complexities arising during convergence in numerical modeling [28]. In contrast, for modeling phase transitions in complex alloy systems, a larger phase change interval may play a crucial role in achieving stable numerical convergence. Hence, a fine-tuned (fitted) free energy function can be employed in such scenarios to model a multicomponent system, even with fewer energy-temperature thermodynamic data points available. In modeling phase transitions during an additive manufacturing process of a multicomponent system (with  $N$  elements), the free energy will be a function of

**Table 1**

Coefficients of thermodynamic constants for the Free energy expressions.

Coeff.	LIQUID	FCC	Unit	Coeff.	LIQUID	Unit	FCC	Unit
$A_\theta$	1337	300	J/mol	$A_\psi$	24.9435	J/mol K	24.9435	J/mol K
$B_\theta$	24474	515	J/mol	$B_\psi$	126.6874	K	126.6874	K
$C_\theta$	16.2	-46.2	J/mol K	$C_\psi$	-0.12027	–	6103.6566	J/mol
$D_\theta$	24.5	-13.5	J/mol K	$D_\psi$	19700	K	-0.001281	J/mol K <sup>2</sup>
$E_\theta$	0.00214	0.1985	1/K	$E_\psi$	14.917	–	-4.02×10 <sup>-7</sup>	J/mol K <sup>3</sup>
$F_\theta$	0.04512	-0.001	J/mol K <sup>2</sup>	$F_\psi$	0.00067	J/mol K <sup>2</sup>	1.55×10 <sup>-6</sup>	JK <sup>11</sup> /mol
$G_\theta$	1.9×10 <sup>-5</sup>	2.0×10 <sup>-5</sup>	J/mol K <sup>3</sup>	$G_\psi$	326.3861	J/mol	-2.27×10 <sup>18</sup>	JK <sup>5</sup> /mol
$H_\theta$	-17.4	-0.001	JK/mol	$H_\psi$	–	–	-2.0566	J/mol K
$T_0$	2662	121	K	$I_\psi$	–	–	9.8072	J/mol K
$T_{th}$	10.412	9.03	–	$J_\psi$	–	–	3898.778	J/mol

temperature and composition (N-1 components) variables. In this case, further incorporation of the composition variable is required to be associated with the fitted expressions.

Whereas, in the presence of a thermodynamic database (.TDB) file, we can extract and implement the free energy expression directly into a FEM solver tool such as the MOOSE Framework with a simple Python script to formulate the necessary temperature-dependent free energy expression syntax. The Python script, in addition to the MOOSE application ("tumbleweed") developed for the current work, is available at: [29, 30]. Using the direct expression from the TDB file not only makes the simulation thermodynamically consistent but also results in highly accurate numerical solutions. As observed in Figure 2(b), the near absence of a phase change interval suggests that there is a very narrow temporal range over which multiple phases co-exist, which results in swift interpolation of material and phase-dependent properties, enhancing the numerical stability of the model.

## 5. Heat Source types of Laser Beam

Due to its standard mathematical formulation and simple beam shape, the Gaussian laser beam is the most widely used beam profile for numerical modeling of laser-based melting-solidification phenomena in additive manufacturing processes [31, 32, 33]. The Gaussian beam exhibits a peak amplitude at the center, with intensity decaying exponentially outward, resulting in a high thermal gradient across the domain that significantly influences microstructure evolution [34]. However, in practical applications, a beam that generates uniform heating of the specimen is often desired, as it contributes to a reduced thermal gradient. To address this, alternative beam profiles have been developed, such as the Flat-Top beam, where the top of the Gaussian profile is truncated to create a flat, hat-like shape. Another alternative is the Ring-shaped beam, in which the heat energy is distributed in a ring pattern with no intensity at the center and peak intensity at a specific annular region [35]. Unlike the Gaussian and Flat-Top profiles, where heat transfers radially outward from the center, the Ring beam's heat distribution occurs inward from the outer ring toward the center. A unique beam profile combining features of both the Gaussian

and Ring beams is the Bessel heat source, where the central beam has a Gaussian profile, and multiple rings extend outward at distances determined by the zeroth-order Bessel function [36].

Experimentally, it has been observed that different laser beam profiles generate different microstructures in additively manufactured samples. For example, Galbusera et al. [37] reported that adjusting the shape of the laser beam affects the melt pool's aspect ratio and depth-to-thickness ratio, which further influences the mechanical properties of the printed product. Similarly, Wischeropp et al. [38] found that using a donut-shaped beam profile resulted in fewer defects during Selective Laser Melting (SLM) of AlSi10Mg. In another study, Tumkur et al. [39] observed that Bessel beams provide better control over melt pool dynamics compared to Gaussian beams, leading to reduced porosity, fewer keyhole defects, and improved mechanical performance. From these studies it can be established that the beam shape plays crucial role in determining the microstructural evolution and mechanical properties of additively manufactured parts. Hence, the computational modelling of different laser beam shapes becomes essential in order to acquire in-depth detail insights such as phase transformation and heat distribution which is challenging to study by experiments alone. Additionally, the cost, efficiency and optimization of laser process parameters can be significantly improved through the computational modelling which can be used in experimental setups. Further, with latest Machine Learning capabilities, we can utilize the computational models to predict different features such as defects, meltpool characteristics, phase transformation ahead in time and take an action to course-correct the process parameters to achieve the required final product with digital twin models.

With such insights, the need for accurate computational modeling of different laser heat source types, along with comparisons based on a set of fixed process parameters, becomes essential. This work, therefore, provides a comprehensive comparison between four laser beam profiles: Gaussian, Flat-Top, Ring, and Bessel heat sources. We proceed by modeling a laser-aided phase field simulation for microstructural evolution in a pure Au system. The comparison is conducted under the same laser process parameters, including laser power (P), outermost effective laser beam

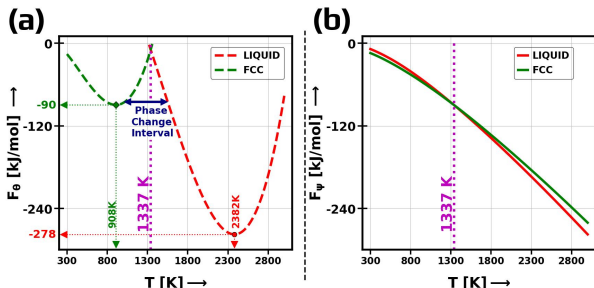


**Figure 2:** Plot depicting the graphical representation of two types of free energy expression used for the phase field simulation of laser processed unary Au system. In (a) the graph showcases the free energy expression based on higher order polynomial-logarithmic functions obtained from thermodynamic data fitting also referred as *fine-tuned expression* represented by  $F\theta$  in Equation 12. The two curves in dashed green and red colors in (a) corresponds to FCC and LIQUID phases of unary Au system respectively. The curve indicates the FCC phase as more stable phase below the melting temperature of 1337 K with the global minima at around 908 K whereas, to the right of the 1337 K vertical line, LIQUID phase is highly stable with a global minima at around 2382 K. The gap between FCC and LIQUID curves at around 1337 K is recognised as Phase Change Interval where the phase transition is expected to occur. This gap also indicates the diffused zone between two phases where both phases can co-exists and is the result of fitting expressions. Whereas, in (b) the free energy expression extracted directed from the '.TDB' file is plotted with respect to Temperature, this expression  $F\gamma$  is referred as TDB based expression in the paragraph sections represented by the Case Equation 12. Similar to (a) the red colored curve represents the LIQUID phase with lower free energy values in the temperature range above 1337 K while green curve indicates the FCC phase which is more stable than LIQUID phase below melting temperature. The intriguing aspect of TDB based free energy plot is the absence of phase change interval representing a rather small window of temperature where the phase transformation occurs near the melting temperature. Such presence and absence of phase change interval in (a) and (b) differentially dictates the rate of information relay of thermal history to the structural evolution making a striking difference in the overall simulation results.

radius, constant coefficients ( $C_a, C_b$ ), and consistent material properties such as absorptance ( $\alpha$ ) and absorption coefficient ( $A$ ). With these different heat source types, we analyze and quantify the melt pool shape, its area, internal flow, and temperature distribution across the domain. Through phase field modeling, we observe a clear distinction between heat and mass diffusion, as well as a lead-lag dynamic between the two fronts. The mathematical expressions describing the four laser beam profiles are discussed in the subsequent sections.

### 5.1. Gaussian Beam

The Gaussian laser beam profile is one of the most popular and widely used laser heat sources in computational modeling of heat transfer. It is commonly applied in numerical modeling for additive manufacturing processes

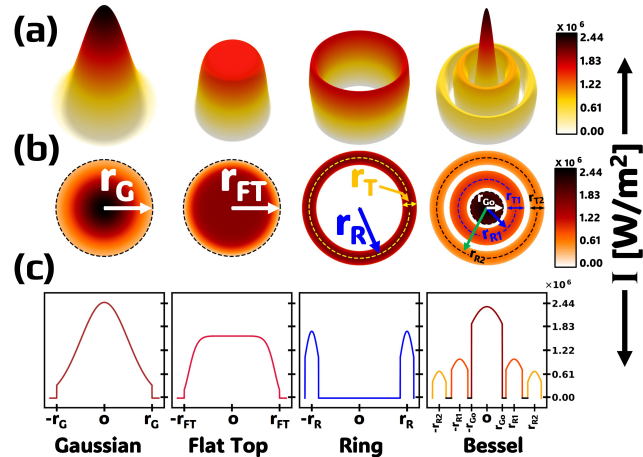


**Figure 3:** A visual demonstration of four different laser beam profiles: Gaussian, Flat-Top, Ring and Bessel used in the study for laser aided phase field simulation of unary Au system. (a) 3D visualization of laser intensity for four beam shapes with an equivalent outer radius of 70  $\mu\text{m}$  [30]. The peak intensity at the centre of Gaussian beam is calculated to be  $2.44 \times 10^6 \text{ W/m}^2$  whereas for Flat-Top, Ring and Bessel beams are  $1.58 \times 10^6 \text{ W/m}^2$ ,  $1.70 \times 10^6 \text{ W/m}^2$  and  $2.33 \times 10^6 \text{ W/m}^2$  respectively as depicted by the colorbar. (b) Showcases the top view of the laser intensities for the four corresponding beams of (a). The Gaussian and Flat-Top beam radius is represented by  $r_G$  and  $r_{FT}$  similarly,  $r_R$  and  $r_T$  denotes the Ring beam radius and thickness of the ring. For the Bessel beam with one central beam with two outer ring beams, the central beam radius is denoted by  $r_{G_0}$ , whereas two ring beams radius are  $r_{R_1}$  and  $r_{R_2}$  with respective ring thickness of  $r_{T_1}$  and  $r_{T_2}$  as shown in the (b). The side view of the irradiance profile of laser sources showcasing the intensity radially outwards is presented in (c) with y-axis representing the irradiance level and x-axis representing the radial distance from the centre of the beam.

such as Selective Laser Melting (SLM), Laser Powder Bed Fusion (LPBF), and even in some laser welding simulations [40, 41, 42]. This beam profile is mathematically simple and well-defined, with an intensity distribution that peaks at the beam center and decays radially outward, forming a Gaussian or bell-shaped curve. Due to the peak irradiance at the center, heating is maximized at the beam core, creating a steep outward temperature gradient. This characteristic carries the risk of overheating or even material vaporization, which can lead to the formation of keyholes and voids [43, 44]. The Gaussian beam profile is particularly useful for materials requiring higher power density to achieve a deeper melt pool regime [45] or for applications such as laser cutting and welding processes [46, 47, 48]. The irradiance from the Gaussian laser beam ( $I_G$ ) is expressed in Equation 13 [36, 49].

$$I_G = \frac{C_a P \alpha}{\pi r_G^2} \exp \left[ -C_b \left( \frac{r^2}{r_G^2} \right) \right] \quad (13)$$

where  $r_G$  is the effective Gaussian beam radius, defined at the radial distance on the beam cross-section where the irradiance (power density) drops to  $\frac{1}{e^2}$  of that at the center of the laser beam. ‘P’ represents the laser power, and  $\alpha$  is the efficiency of laser power conversion into heat.  $C_a$  and  $C_b$  are constant coefficients. The numerical values of these coefficients are provided in Table 2. A visual representation of the Gaussian laser beam is shown in the first column of Figure 3, with a 3D view in (a), and top and side views in (b) and (c), respectively.

## 5.2. Flat Top | Super Gaussian Beam

The Flat-Top laser beam represents a beam profile with a uniform intensity distribution within a circular beam radius and a sharp drop in intensity at the edges. It can also be visualized as a Gaussian beam with a truncated top, resembling a hat-shaped profile. The primary advantage of the Flat-Top beam profile is that it delivers a uniform energy distribution across the beam diameter, resulting in homogeneous heating of the material [49, 50]. This leads to minimized localized overheating and improved control over defect formation during the melting-solidification process. Flat-Top laser heat sources are also sometimes referred to as Super Gaussian Beams, with a Gaussian order ( $k$ ) greater than 1, when the Gaussian order equals one, the beam behaves as a standard Gaussian Beam [36]. The Irradiance ( $I_{FT}$ ) equation for Flat-Top type laser source is given by the following expression 14 [36, 51, 49, 52].

$$I_{FT} = \frac{C_a^{1/k} k P \alpha}{\pi r_{FT}^2 \Gamma(1/k)} \exp \left[ -C_b \left( \frac{r^2}{r_{FT}^2} \right)^k \right] \quad (14)$$

In the equation,  $r_{FT}$  denotes the effective Flat-Top beam radius, ‘P’ is the beam power,  $C_a$  and  $C_b$  are constant coefficients, and ‘ $k$ ’ is the super-Gaussian order, set to 4.2 in this work [36].  $\alpha$  is the laser beam heat conversion efficiency, the values of these coefficients are listed in Table 2. A visual representation of the Flat-Top laser beam is shown in the second column of Figure 3, with a 3D representation in 3(a), top view in 3(b), and side view in 3(c).

## 5.3. Ring Beam

The ring laser beam is another widely used beam profile; its unique ring structure creates a distinct irradiation pattern. This beam shape forms a closed circular loop with maximum beam intensity around the circumference of the ring, with a dim center. The visualization of this beam type in both 3D and 2D is presented in Figure 3, in the third column. The ring laser beam distributes heat from the outer ring toward the center, creating a uniform heating effect that helps reduce thermal defects [53, 54]. In our study, we consider an isotropic heat distribution for the ring laser beam, with heat spreading uniformly in all directions. The ring beam profile introduces an additional process parameter, the ring width, which can be useful in controlling energy distribution across the domain [55, 56]. The mathematical expression for

the Irradiation in ring beam profile is given in Equation 15 [34, 35, 57, 58].

$$I_R = \frac{C_a P \alpha}{\pi r_T^2 Y(r_R, r_T)} \exp \left[ -C_b \left( \frac{(r - r_R)^2}{r_T^2} \right) \right] \quad (15)$$

where  $P$  is the power of the laser,  $r_R$  is the ring beam radius,  $r_T$  is the ring thickness (width),  $C_a$  and  $C_b$  are constant coefficients, and  $\alpha$  is the absorptance. The numerical values of these processing parameters are listed in Table 2. Moore et al. [34] describes the ‘Y’ function as a distribution function that defines the radial distribution of irradiation. It incorporates a localized exponential decay term and a complementary error function that accounts for the effects of the ring radius and ring thickness on the beam’s profile, given as follows:

$$Y(r_R, r_T) = \exp \left( \frac{-r_R^2}{2r_T^2} \right) + \frac{r_R}{r_T} \sqrt{\frac{\pi}{2}} \operatorname{erfc} \left( \frac{-r_R}{\sqrt{2}r_T} \right)$$

## 5.4. Bessel Beam

The Bessel beam profile consists of a core beam with concentric ring beams extending radially outward, with irradiance gradually decreasing along the radius. In this study, we consider a central Gaussian-type beam with two concentric ring beams, where each beam radius corresponds to the zeros of the zeroth-order Bessel function. In the literature, the radius of the central beam in a Bessel beam is often defined as the radial distance at which irradiance drops to  $\frac{1}{e^2}$  of the beam spot’s peak irradiance [59]. However, here we define the radius of the central beam as the location of the first zero of the Bessel function. For the radii of the two concentric ring beams, we use the second and third zeros of the Bessel function. The visualization of the Bessel beam is shown in the fourth column of Figure 3, with the 3D, top, and transverse profiles displayed in 3(a), (b), and (c), respectively. As this study aims to compare the effects of four laser beams under similar processing parameters, the total power of the Bessel beam is divided among the three beams, with attenuation coefficients  $a_0$ ,  $a_1$ , and  $a_2$ , as given in the mathematical expression in Equation 16 for the Irradiance ( $I_B$ ) [36, 59].

$$I_B = \frac{C_a a_0 P \alpha}{\pi r_{G_0}^2} \exp \left[ -C_b \left( \frac{r^2}{r_{G_0}^2} \right) \right] + \frac{C_a a_1 P \alpha}{\pi r_{T_1}^2 Y(r_{R_1}, r_{T_1})} \exp \left[ -C_b \left( \frac{(r - r_{R_1})^2}{r_{T_1}^2} \right) \right] + \frac{C_a a_2 P \alpha}{\pi r_{T_2}^2 Y(r_{R_2}, r_{T_2})} \exp \left[ -C_b \left( \frac{(r - r_{R_2})^2}{r_{T_2}^2} \right) \right] \quad (16)$$

here,  $C_a$  and  $C_b$  are the constant coefficients,  $P$  is the power of the laser,  $\alpha$  is the absorptance. The radius of the central Gaussian beam is denoted by  $r_{G_0}$ , while the radii

**Table 2**  
Laser processing parameters.

Coeff.	Gaussian	Flat-Top	Ring	Bessel	Unit
P	25	25	25	25	mW
$C_a$	2	2	2	2	–
$C_b$	2	2	2	2	–
$\alpha$	0.75	0.75	0.75	0.75	–
$r_G$	70	–	–	–	μm
$r_{FT}$	–	70	–	–	μm
k	–	4.2	–	–	–
$r_R$	–	–	70	–	μm
$r_T$	–	–	20	–	μm
$r_{G_0}$	–	–	–	22.65	μm
$r_{R_1}$	–	–	–	40	μm
$r_{T_1}$	–	–	–	30	μm
$r_{R_2}$	–	–	–	70	μm
$r_{T_2}$	–	–	–	20	μm
$a_0$	–	–	–	0.1	–
$a_1$	–	–	–	0.5	–
$a_2$	–	–	–	0.4	–

of the two concentric rings are represented as  $r_{R_1}$  and  $r_{R_2}$ , with their respective beam thicknesses given by  $r_{T_1}$  and  $r_{T_2}$ . The three attenuation coefficients,  $a_0$ ,  $a_1$ , and  $a_2$ , are unitless values that sum to 1, dividing the total supplied power P into  $Pa_0$ ,  $Pa_1$ , and  $Pa_2$ , respectively. The numerical values of these process parameters are provided in Table 2.

## 6. Material Properties

In a phase-field simulation involving laser-induced phase transformations, the material properties of the different phases play an important role in phase evolution itself. Properties such as phase mobilities, thermal conductivities, densities, and specific heat capacity are highly influential in determining the overall microstructural evolution and the kinetics of the reaction. To accurately model the phase transformation phenomenon, these properties should be defined properly and precisely, as they themselves depend on temperature. Therefore, using constant values for thermo-physical properties in a non-isothermal laser processing simulation results in a highly inaccurate and unreliable model. To address this issue, we utilize thermodynamic expressions that define the values of material properties for a unary Au system as functions of temperature. Furthermore, these material properties are classified according to the individual phases under consideration. Using the interpolation function described in Equation 1 of Section 3, the FEM solver accurately adjusts the material properties for the respective phases at specified temperatures. Table 3 presents the mathematical expressions for the temperature dependence of material properties: density ( $\rho$ ), specific heat capacity ( $C_p$ ), thermal conductivity ( $k_{th}$ ), phase mobilities ( $M$ ), and melt pool viscosity ( $\mu_{LIQ}$ ) for the two distinct phases, LIQUID and FCC. It should be noted that this work assumes the thermal conductivity of both phases to be isotropic in nature. The driving force, or the free energy of the system governing phase evolution during laser processing, is another key

material property that depends on the composition and temperature of individual phases. In a unary system, the composition is uniform across the entire computational domain, so the free energy depends solely on temperature. As discussed in Section 4, we consider two versions of free energy expressions: a fitted expression and an expression extracted from a thermodynamic database (TDB). These two temperature-dependent free energy expressions are listed in Equation 12. It is well known that phase field simulations are generally associated with a diffused interface model, so we introduce a mushy zone as an interface between the solid and melt pool regions, where the viscosity of this zone ( $\mu_{adj}$ ) is given by Equation 17. Similarly, in the study the absorption coefficient of gold is taken to be  $8.5 \times 10^7 \text{ m}^{-1}$  [60].

$$\mu_{adj} = 10 \times \mu_{LIQ} \times [h_{LIQ} \times (1 - h_{LIQ})] \quad (17)$$

here,  $h_{LIQ}$  refers to the interpolation function that governs the switching action between the FCC and LIQUID phases at the interface, while  $\mu_{LIQ}$  represents the temperature-dependent viscosity of the meltpool, with the expression provided in Table 3.

## 7. Machine Learning and Digital Twin

The major challenge of the additive manufacturing process lies in quantifying the laser-microstructure interaction [63, 64]. Even with high-speed thermal cameras, it is difficult to capture the detailed intricacies of phase transformations that occur in real-time during the 3D printing process. The size, area, and depth of the meltpool formed, the heat-affected zone, flow within the meltpool, differences in thermal and phase diffusions, and the solidification rate all play important roles in determining the quality and desired properties of the additively manufactured part [65]. During an additive manufacturing process, as materials are melted and fused together, phase transformations and crystal structure changes occur, resulting in variations in physical and mechanical properties. A numerical model of such phenomena can significantly aid in understanding the material process-structure-property relationships. However, a major hindrance to numerical models is the computational cost associated with developing multiple models that correlate with multiple processing parameters.

As the practice of pairing experiments with mathematical models in real time has begun in many industries, enabling a higher level of process control [66], there is a growing need for a computational model that can operate in tandem with additive manufacturing experiments, delivering process-property information at the same pace.

This digital version of the experimental setup offers greater leverage in understanding the in-depth physical phenomena that occur during laser processing by quantifying key properties. This enables us to course-correct experimental pathways if needed, which is the basic concept of a Digital Twin. Such a digital twin requires a computational model capable of predicting outcomes instantaneously based

**Table 3**  
Material Properties

Properties	Phase	Expression	Reference
Density ( $\rho^i$ )	LIQUID	$19325.28 - 1.44T$	[60]
	FCC	$19657.60 - 1.20T$	[60]
Specific Heat ( $C_p^i$ )	LIQUID	$158 + 5.08 \times 10^7 \exp(-0.0114T)$	[61]
	FCC	$132 + 2.5 \times 10^{-5}T^2 - 0.011T$	[61]
Thermal Conductivity ( $k_{th}^i$ )	LIQUID	$100 + 0.027397T$	[60]
	FCC	$338.91 - 0.0693T$	[60]
Phase Mobility ( $M^i$ )	LIQUID	$3.15 \times 10^{-15} \exp\left(\frac{-1073.15}{8.31T}\right)$	[18] unpublished
	FCC	$3.38 \times 10^{-17} \exp\left(\frac{-1165.84}{8.31T}\right)$	[18] unpublished
Viscosity ( $\mu_{LIQ}$ )	LIQUID	$\exp\left(-0.1990 + \frac{2669}{T}\right)$	[62]

on real-time data input from experiments. Although FEA models can accurately simulate multiphysics phenomena, their computational time far exceeds that of experiments. FEA simulations can take days or even weeks to complete, and a major limitation is that they must be rerun if even a single process parameter changes. Therefore, every small variation in processing parameters requires a separate FEA simulation, which increases computational cost and makes real-time tracking in additive manufacturing impractical. At the intersection of optimal computational time and predictive accuracy, a machine learning model trained on simulation-generated data can be at the forefront of Digital Twin applications. This work provides a foundation for constructing a digital twin model and suggests a pathway for designing one that can monitor experimental setups and track multiple variables in real time. These variables can include meltpool shape, area, depth, phase transformations, flow velocity inside the meltpool, and the behavior of phase diffusion relative to thermal diffusion. Such data can be predicted with a single input to the Digital Twin, such as a surface temperature profile provided by a thermal camera.

Further, we present a machine learning model capable of predicting the evolution of the meltpool (LIQUID phase) in a 2D image format when provided with temperature distribution data as input. This trained model can be stored on a portable, lightweight mini-computing device, such as a *Raspberry Pi* [67], to predict phase evolution in real time during experiments, using input from an Infra-Red camera attachment that records the specimen surface's thermal history data. Additionally, we have developed a web application that allows users to input temperature distribution data in *numpy array* [68] format and predict the meltpool phase for the specified thermal data of a unary Au system. This web application can be extended to multiple alloy systems by training separate machine learning models for each alloy, enabling a Digital Twin that can be rapidly adapted to different applications and needs with multiple machine learning models.

## 7.1. Training Data and Model Architecture

The accuracy of any machine learning model depends on the volume of training data and on proper hyperparameter

**Table 4**  
Model Hyperparameters

Hyperparameter	Value
Batch Size	13
Learning Rate	$1 \times 10^{-4}$
Number of Epochs	50
Input Channels	1
Output Channels	1
Loss Function	BCEWithLogitsLoss
Optimizer	Adam
Random State	69
Test Split	10%
Validation Split	10%

tuning of the model architecture. In this study, we utilize data generated from multiple FEM simulations, varying both the laser beam profile and the free energy function.

From eight distinct phase-field laser simulations, as described in Sections 4 and 5, a total of 3220 observations of temperature distribution and corresponding phase evolution were extracted from the exodus file generated by the FEM solver. The extracted data were converted into a Numpy 3D array in the format (x-coordinate, y-coordinate, time), containing numerical values for temperature and phase information at each coordinate and time step. The organized data array was randomly divided in an 80:10:10 ratio for training, testing, and validation purposes. For training and prediction, the input to the machine learning model, referred to as the Input Image, is an array of temperature distribution within the domain (x-coordinate, y-coordinate) at a specific time (e.g.,  $t$ ). The model's output, referred to as the Output Label, is an array containing information about the meltpool phase coordinates at the same time instance ( $t$ ). As only two phases are considered: LIQUID and FCC, each can be represented by a single variable,  $\eta$  and  $1 - \eta$ , respectively. To enhance computational efficiency, the model output, representing LIQUID and FCC phases, is expressed as 1 or 0 at each spatio-temporal point. This unique system uses the temperature distribution as an input for predicting the spatio-temporal coordinates of the meltpool or FCC phase, thus presenting a binary classification problem.

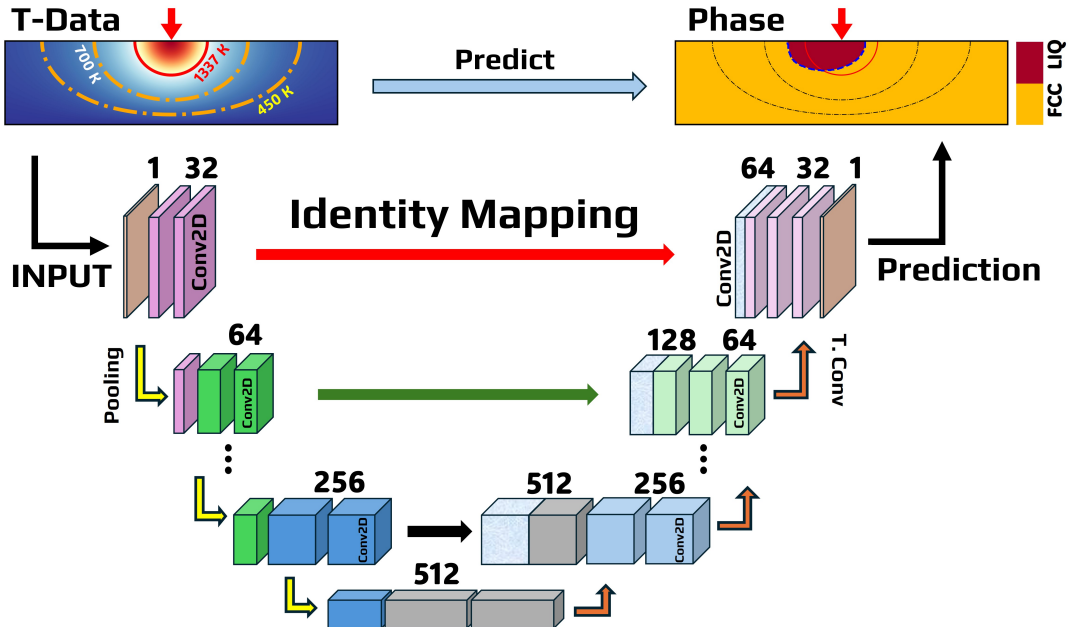


**Figure 4:** A schematics illustrating the tailored U-Net machine learning architecture to predict the phase dynamics based on the temperature distribution (T-Data) across the input domain. The model is intended to process the thermal data as an input going through multiple encoding and decoding blocks consisting of several convolutional layers and max-pooling inbetween to extract the features within the input data that is correlated with the phase profile for corresponding T-Data. The model architecture at the first half reduces the spatial dimension and increases the data channel at every encoding block as illustrated by 1, 32, 64, 124, 256, 512 channels. At the bottleneck, the end of encoding block and beginning of decoding block, the detailed features in input data is transferred to decoding blocks moving upwards. At every decoding block the channels are decreased from 512, 256, 124, 64, 32 to 1 whereas, the spatial dimension is increased by mapping the spatial identity from corresponding encoder to decoder block as shown by arrows pointing from left to right. Finally by the end of decoder block, the model predicts output segmenting the LIQUID and FCC phase in a equal spatial coordinate space with single channel data. During the training process thousands of T-Data observations are fed to the model and every prediction of phase is equated with actual phase evolution data from phase field simulation and the necessary training parameters (weights and bias vectors) are adjusted accordingly to minimize the differences between predicted result and ground truth generated phase data.

For a binary classification problem to segment the LIQUID phase from FCC, we employed the U-Net architecture [13], which is popularly used in image segmentation tasks. Here, the two phases, LIQUID and FCC, are processed as two segments within the computational domain at each time step, with the model trained to identify the LIQUID phase region. The U-Net architecture is a convolutional neural network with encoder and decoder blocks arranged in a symmetrical fashion. The schematic of the model architecture used in this study is presented in Figure 4, while the hyperparameters used in the machine learning process are listed in Table 4. A detailed model architecture, including fully functional code with encoder, bottleneck, and decoder blocks, along with the corresponding convolutional, max-pooling, upsampling layers, and individual channels, is available on the [GitHub](#) page further mentioned in Section 13. The accuracy, loss, and prediction results for training, testing, and validation are further discussed in Section 8.3.

## 8. Result and Discussion

In this section, we present extended insights into the results obtained from phase-field simulations and machine

learning model predictions. In Section 8.1, we examine the thermo-phase response to different energy models or expressions used during laser-induced phase-field simulations. The microstructural evolution of the melt pool, its area, temperature distribution across the simulation domain, and variations in the thermal profile under different laser beam profiles are discussed in Section 8.2. Finally, in Section 8.3, we discuss the predictions from a machine learning model trained on microstructure evolution data generated by phase-field simulations. Here, we elaborate on the model's capability to accurately predict laser-induced multiphase phenomena. Additionally, we provide insights on utilizing results from a simple, rapid, and effective heat transfer FEM simulation to predict phase transformations induced by heat input using the trained ML model, with a visual demonstration.

### 8.1. Phase Response to Energy Models/Expressions

Phase evolution is a complex phenomenon primarily driven by the free energy of the system, a phase with minimum free energy at a given temperature dictates the stability moving forward temporally. This study attempts to compare

the response of phases, their stabilities and transitions in-addition to the thermal history, for two sets of driving force expressions in a laser aided phase field simulation. Looking at the Graph 2, we can notice that for fitted expression of 2(a) the free energy curves for two phases are distinct parabolic in nature intersecting near the melting point of Au creating a phase change gap between them, whereas for TDB based free energy curves in 2(b) cross each other at same temperature without any gap between the LIQUID and FCC curves.

The evolution of LIQUID phase with fine-tuned free energy expression ( $F_\theta$ ) in the phase field simulation is visually distinct from that of TDB based expression which can be observed in Figure 5. The initial LIQUID phase of area  $2500 \mu\text{m}^2$  grows to a semi-circular shape exactly matching the contour of 1337 K temperature on the domain at around 1s into the simulation as shown in Figure 5(a). As the simulation progresses, the LIQUID (meltpool) follows the temperature contour of 1337 K refer Figure 5(b) until the heat source is turned off. Whereas the result of simulation with TDB extracted expression ( $F_\psi$ ) depicted in Figure 5(c), it can be seen that the meltpool is not fully developed at time  $t = 1\text{s}$  as compared (a). The visible distinction in meltpool geometry between the (a) and (b) is that for  $F_\theta$  meltpool front and meltpool shape exactly lines up with the contour of melting temperature (1337 K) whereas for  $F_\psi$  the thermal front of 1337 K leads the LIQUID phase front. While the Figure 5 shows the phase evolution on application of Gaussian laser beam profile, similar result and distinction is observed in LIQUID phase evolution for all other three laser beams. The result from other three beams is presented in Appendix A.

Another aspect where a significantly different observation can be made between simulations with  $F_\theta$  and  $F_\psi$  is in the range of maximum temperature measured inside the domain. Plot 6 depicts the bar graph showcasing the range of peak temperatures at the top surface of the computational domain, over the simulation duration for fine-tuned free energy 6(a) and TDB extracted free energy 6(b). It can be noted that for any given laser beam profile, the greater temperature in the domain is observed for simulation with fine-tuned free energy ( $F_\theta$ ) compared to TDB based expression ( $F_\psi$ ). In Figure 6(a), Gaussian beam profile produces an average peak temperature of 2958 K over the total computational time, whereas in 6(b) the mean peak temperature for Gaussian beam is 2880 K. Another noticeable difference in the plot is the range of maximum temperature that the domain attains over time. For simulation with  $F_\psi$  the range of highest temperature attained by the domain is bigger compared to the simulation with  $F_\theta$  indicated by the wider error-bars for all four laser beam profiles in Figure 6(a) and (b).

On analysing, it is observed that the free energy expression plays another crucial role in the meltpool / LIQUID phase i.e. on its flow velocity. Figure 7(a) and (b) shows the flow velocity for two different laser beam profiles Bessel and Ring at mid-simulation (time  $t = 12.5\text{s}$ ) for the fine-tuned energy expression ( $F_\theta$ ). Whereas, Figure 7(c) and (d) relates to simulation with TDB based expression ( $F_\psi$ ) for

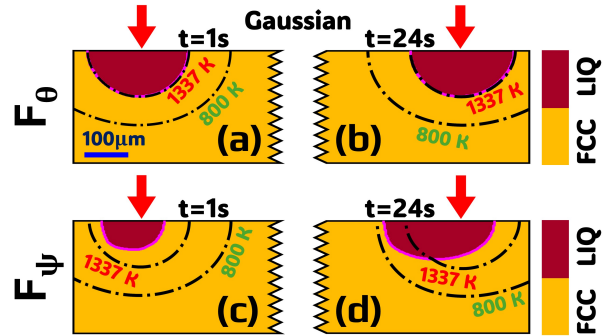


**Figure 5:** The illustration of phase evolution in unary Au system on being irradiated by the Gaussian laser beam profile with power of 25 mW at a scan speed of  $30 \mu\text{m}/\text{s}$  from top left of the computation domain to top right. The subplots (a) and (b) represents the simulation at two time stamps at  $t=1\text{s}$  and  $t=24\text{s}$  respectively for the phase field simulation with fine-tuned free energy expression ( $F_\theta$ ). It can be noted at both time stamps the LIQUID phase represented by dark red color aligns perfectly with the melting temperature contour line of 1337 K. Whereas (c) and (d) represents the phase evolution resulted from simulation with TDB-file based free energy expression ( $F_\psi$ ). The key difference in phase evolution with fine-tuned free energy expression and TDB-file extracted expression is on the gap that is present in second between the leading melting temperature contour line of 1337 K and LIQUID phase front. The positional time lag between these two fronts can be attributed to the difference in phase diffusion and thermal diffusion with thermal diffusion leading the phase. Other key difference in LIQUID phase evolution with two free energy considerations is that at time  $t=1\text{s}$ , the meltpool is fully developed with an area of  $18484.18 \mu\text{m}^2$  for  $F_\theta$  compared to an area of  $7575.42 \mu\text{m}^2$  for  $F_\psi$ . The difference in meltpool area evens out reaching a mean of  $\approx 17800 \mu\text{m}^2$  near the end of simulation as depicted in (b) and (d) respectively although the actual shape of meltpool is drastically different between two simulation results. The phase evolution simulation results from Flat-Top, Ring and Bessel beams are presented in Appendix A

same beam profiles (Bessel and Ring) at the same time. From the figure, it can be noted that for  $F_\theta$ , the peak flow velocity is  $81.17 \mu\text{m}/\text{s}$  for Bessel heat source and  $18.90 \mu\text{m}/\text{s}$  for Ring beam. Similarly, for  $F_\psi$  based simulation, the peak velocity incase of Bessel beam profile is about  $56.29 \mu\text{m}/\text{s}$  whereas for Ring heat source it is  $23.71 \mu\text{m}/\text{s}$  respectively. We found that the Ring laser beam acts as an exception to other beam studied, as for it the peak flow velocity during the simulation is higher for TDB based expression  $F_\psi$  compared to fine-tuned ( $F_\theta$ ) one. This phenomenon is further discussed in Section 8.2.

In the case of temperature distribution and peak temperature reached by the computational domain, the role of different the free energy expressions becomes quite distinct. First of all, the major noticeable distinction in temperature-meltpool profile as a result of different free energy expressions is, for  $F_\psi$ , there exists the physical gap between leading thermal front of melting temperature (1337 K) and actual meltpool front as shown in Figure 8(c) and (d) indicated

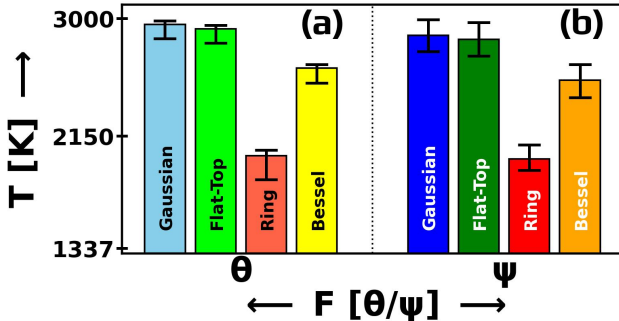


**Figure 6:** A bar graph comparing the average peak temperature measured at the top surface of the computational domain when the laser transverses from left to right during the phase field simulation. In (a), the mean peak temperature from phase field simulation involving the fine-tuned free energy ( $F_\theta$ ) expression. From the plot it is observed that the Gaussian beam profile increased the temperature of the domain to a maximum peak of 3061.58 K followed by Flat-Top, Bessel and Ring beam shapes at 3028.92 K, 2748.94 K and 2180.13 K respectively. Similarly, in (b) the plot showcases the peak temperature during the simulation with free energy expression extracted from the TDB file ( $F_\psi$ ). The trend is similar to that of (a) with highest temperature reached during the Gaussian laser beam simulation followed by Flat-Top, Bessel and Ring beam shape with the peak temperature during the whole simulation time measure at 2996.36 K, 2966.37 K, 2680.17 K and 2069.10 K respectively. The key differentiation between (a) and (b) with the use of free energy expression  $F_\theta$  and  $F_\psi$  is that for simulation with fine-tuned free energy expression compounded to an average higher temperature values for all four laser beam profiles to the simulation conducted with free energy expression from a TDB file.

by red contour line for melt pool and black dotted contour lines for temperature. The positional lag between thermal and phase diffusion can be observed only in simulations with TDB extracted free energy ( $F_\psi$ ) while there is no such gap for  $F_\theta$  indicated by red dotted contour lines for melt pool overlapping the white dotted thermal contour line at 1337 K in Figure 8(a) and (b) respectively.

Another exciting phenomenon observed in simulations with  $F_\psi$  is that the temperature distribution at the leading front of the domain (to the right of the laser moving from left to right) is wider than that in lagging part (to the left of the laser). This can be clearly visualized in Figure 8(c) and (d) where the spatial difference between thermal front of 1337 K and 800 K at the top right surface ( $\beta_\psi$  and  $\beta'_\psi$ ) is larger than that in top left surface ( $\alpha_\psi$  and  $\alpha'_\psi$ ) for same temperature fronts. Whereas, for simulation with fine-tuned free energy expression ( $F_\theta$ ), there is no significant difference in thermal contour at leading and lagging fronts i.e.  $\alpha_\theta \approx \beta_\theta$  and  $\alpha'_\theta \approx \beta'_\theta$  in Figure 8(a) and (b) respectively.

## 8.2. Laser Profiles and Phase Dynamics

In this section, we present the discussion about results obtained from phase field simulation coupled with heat transfer physics which initiates the phase transformation.

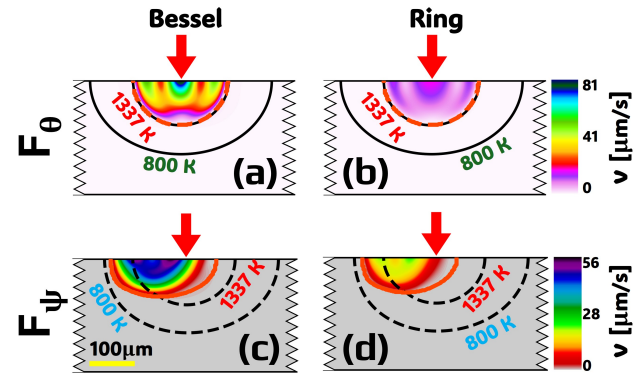


**Figure 7:** The subplots illustrating the velocity profile of melt pool when the laser beam reaches the domain mid point (500  $\mu\text{m}$  from top left corner) at time  $t=12.5\text{s}$  into the simulation for two different laser beam profile with two free energy expressions considered for the study. In (a) and (b) the plots depict the melt pool flow velocity for Bessel and Ring laser beam with simulation conducted with fine-tuned free energy expression ( $F_\theta$ ). Similarly in (c) and (d) the LIQUID phase velocity profile is presented for Bessel and Ring laser irradiation for the free energy expression ( $F_\psi$ ) implemented directed from the TDB file. The noticeable difference in flow velocity due to the application of Bessel and Ring beam profile is the range of velocity inside the melt pool is comparatively higher for simulation with Bessel beam to that of Ring beam for both free energy expression. For  $F_\theta$  expression, the maximum velocity inside the LIQUID phase for Bessel type laser beam is calculated to be around 81  $\mu\text{m/s}$  to that of 18.90  $\mu\text{m/s}$  for Ring beam whereas for simulation with  $F_\psi$  expression, the respective maximum flow velocity are 56  $\mu\text{m/s}$  and 23.71  $\mu\text{m/s}$  for Bessel and Ring beam respectively. In case of the difference seen in velocity profile with respect to free energy expression type, it can be observed that for Bessel beam fine-tuned free energy expression results in an overall higher flow velocity in contrast for Ring beam the TDB based free energy produced a greater flow inside the melt pool compared to fine-tuned expression.

Specifically, here we elaborate with extensive details on how the different laser beam profiles changes the phase dynamics. As mentioned in Section 5 the four beam profiles considered for the study are: Gaussian, Flat-Top, Ring and Bessel. And the effect of each of them on phase dynamics is carried out on equal laser processing parameters i.e. laser power, scan speed and effective outer beam radius. In our investigation, we found that among four beam shapes, Ring beam profile behaves uniquely in context of heat distribution and temperature profile. This results in a different trend of melt pool area evolution, LIQUID phase flow velocity and peak temperature attained by the system.

Starting with the temperature distribution and thermal history along inside the simulation domain it is observed that with Gaussian beam, the peak domain temperature is maximum compared to all other three beams. Following the Gaussian beam, Flat-Top laser source with equal beam radius of 70  $\mu\text{m}$  generates second highest peak temperature. For Gaussian beam, the domain reached a peak of 3061.58 K

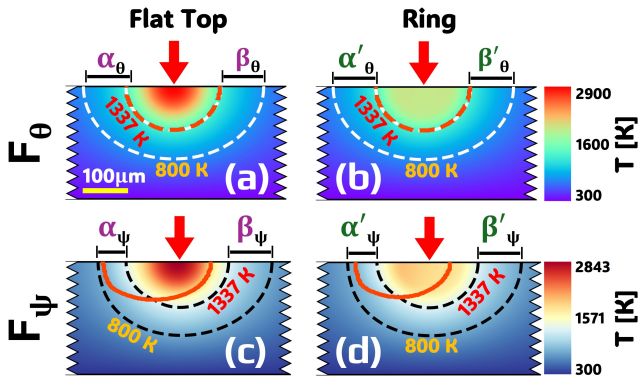


**Figure 8:** A comparative illustration of temperature distribution for Flat-Top and Ring laser beam profile mid simulation at time  $t=12.5\text{s}$  when the laser reaches the exact midpoint of the top surface of computational domain. Subplot (a) and (c) refer to Flat-Top beam profile for simulation conducted under fine-tuned free energy expression  $F_\theta$  and TDB extracted free energy expression  $F_\psi$  respectively where as figure (b) and (d) corresponds to Ring laser beam for  $F_\theta$  and  $F_\psi$  correspondingly. Starting with (a) for the Flat-Top laser beam shape with  $F_\theta$  free energy, the temperature distribution is symmetrical in both leading and trailing edges of temperature contour i.e.  $\alpha_\theta \approx \beta_\theta \approx 97.76\text{ }\mu\text{m}$  with a peak of around 2900 K at the beam centre. Similar is the case for (b) although the temperature distribution across the Ring radius appears uniform with a peak of 1967.28 K, the leading and lagging edges of temperature contours are near symmetrical with values of  $\alpha'_\theta \approx \beta'_\theta \approx 92.27\text{ }\mu\text{m}$ . One of the noticeable visual clue in both (a) and (b) is that the temperature contour line of 1337 K perfectly aligns with the meltpool phase boundary represented by dashed red line which suggest that there is no any lag between phase diffusion front and thermal diffusion front on implementing fine-tuned free energy expression for the phase field simulation. Whereas, in case of free energy expression extracted from TDB file and implemented directly into FEM solver script, there is a noticeable gap between temperature front and phase front depicted by the red contour line for meltpool phase and dashed black line for 1337 K in (c) and (d). In addition, it is observable that there is an asymmetry in thermal contour lines at the leading and trailing fronts in  $F_\psi$  based simulations. In (c) for Flat-Top laser profile, the gap between two selected temperature contour values of 1337 K and 800 K at the leading front  $\beta_\psi$  (94.76  $\mu\text{m}$ ) is greater than trailing front  $\alpha_\psi$  (62.34  $\mu\text{m}$ ) which is the case for (d) as well with values of  $\beta'_\psi$  and  $\alpha'_\psi$  as 94.76  $\mu\text{m}$  and 64.83  $\mu\text{m}$  respectively. The key difference between Flat-Top and Ring beam on imparting heat energy to the computational domain and temperature distribution across is that Flat-Top heat source raises temperature of the domain significantly higher compared to that of Ring laser heat source for any free energy expressions.

and 2996.36 K for  $F_\theta$  and  $F_\psi$  respectively, whereas for Flat-Top, the peak temperatures are 3028.92 K and 2966.37 K for  $F_\theta$  and  $F_\psi$  as shown in Figure 6(a) and (b) in shades of blue and green bars. Similarly, for Bessel beam, the maximum temperature attained by the domain over the simulation are: 2748.94 K and 2680.17 K for  $F_\theta$  and  $F_\psi$  represented by

yellow shades of bars in Figure 6. For these three beam profiles, the peak temperature of the domain are in similar range (over 2500 K) but for the Ring laser beam, the drastic difference can be observed. The red shades of bar in Figure 6 represents the maximum temperature inside the computational model, for simulation with fine-tuned free energy expression  $F_\theta$ , the peak temperature is around 2180.13 K and for TDB free energy expression  $F_\psi$  it is measured to be the lowest of all i.e. 2069.10 K. The low temperature for Ring beam profile can be associated with the way heat energy is distributed inside the system. For Gaussian, Flat-Top and Bessel beam, the presence of central beam makes the energy transfer radially outwards from the centre with a concentrated high irradiance at the centre, but for a Ring beam, the centre of the beam gets near-zero direct irradiance from the source. The heat energy deposited is focused on a circular ring away from the centre hence the heat transfer occurs both inwards to the centre of the beam and outwards of the ring creating a uniform heat distribution which inturns does not let temperature to abruptly rise to peak as compared to other three beam profiles. This can be further noticed in Figure 8(b) and (d) where we can see that the temperature profile is rather uniform and distributed radially around the top surface equally compared to Flat-Top beam in Figure 8(a) and (c) with maximum temperature directly at the centre of the beam.

The temperature profile for other two laser beams (Gaussian and Bessel) at  $t = 12.5\text{s}$  into the simulation i.e., when the laser beam spot reaches middle of the domain, is presented in Figure A2 at Appendix A. For Gaussian and Bessel beam, the thermal distribution profile is near similar to one another with a single main difference being the peak temperature attained by the computational system. The Gaussian beam imparts dense irradiation at the centre of the beam which exponentially decays radially whereas for the Bessel beam, the centre beam and two outer ring beams share the total power supplied in a ratio of attenuation coefficients:  $a_0$ ,  $a_1$ , and  $a_2$ , as expressed in Equation 16 with  $a_0+a_1+a_2=1$ . From the mathematical formulation it can be said that the Bessel beam gets benefits of both Ring and Gaussian profile by varying the values of attenuation coefficients.

Another key insight regarding the difference in laser beam profiles can be understood with the effects beam shape on governing the microstructure and evolution of the phases. For meltpool phase the evolution studied by measuring its area throughout the simulation time. The area of meltpool is tracked at every time iteration during the simulation and a comprehensive overview is prepared. Plot 9 demonstrates the LIQUID phase area growth from the start of the simulation till the end for four types of laser heat sources including the variation of two free energy expression in the phase field setup. From the graph, it can be deduced that for all four heat source with fine-tuned free energy expression ( $F_\theta$ ) the meltpool grows in a similar trend during the simulation with an average area of around  $\approx 16,500\text{ }\mu\text{m}^2$  denoted by green, yellow, navy and brown coloured lines in Figure 9(a),(b), (c) and (d) respectively. Whereas, for the simulation with TDB

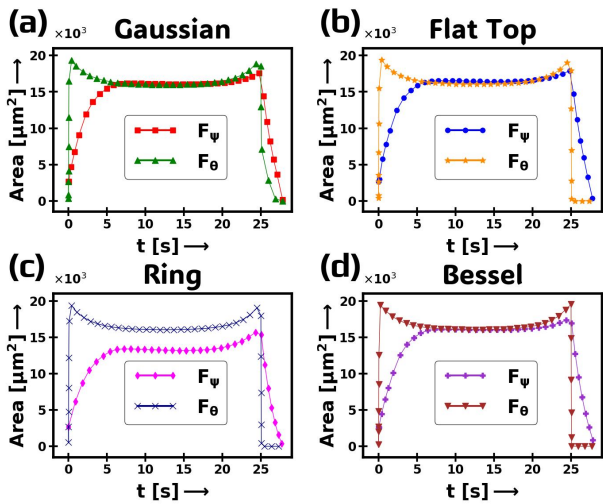


**Figure 9:** The graphs in subplot illustrates the area evolution of melt pool (LIQUID) phase over the simulation duration for four different laser heat source profiles and two types of free energy expressions influencing the melt pool growth for each beam shapes. In (a) the melt pool area growth for simulation performed with Gaussian beam is plotted where it can be observed that for fine-tuned free energy  $F_\theta$  sharply causes the melt pool to rise sharply to a value of  $19422.59 \mu\text{m}^2$  within seconds of simulation and balances out at around  $16497.74 \mu\text{m}^2$  on average till the end as depicted by the green colored line with triangular marker. Whereas, for the simulation with TDB file driven free energy expression  $F-\psi$ , the melt pool area gradually grows without a sudden peaking and settles at around similar area of  $15551.55 \mu\text{m}^2$  throughout the end till the laser is turned off after 25s into the simulation as denoted by the red line with square markers. The similar trend can be observed for Flat-Top in (b) and Bessel beam in (d) with sudden rise in melt pool area for fine-tuned energy expression and gradual increase in LIQUID phase for TDB based expression both averaging around  $16500 \mu\text{m}^2$ . The exception in this trend is visible for Ring laser beam as shown in (c) where, the fine-tuned fitted free energy expression produced an average melt pool area of  $16549.60 \mu\text{m}^2$  (blue colored line with cross symbols) from the beginning of the simulation till the laser is turned off whereas for TDB extracted free energy simulation, the melt pool area is drastically low with an average of  $12967.09 \mu\text{m}^2$  gradually peaking to  $16338.35 \mu\text{m}^2$  depicted by magenta line with diamond markers. A unique difference in evolution of LIQUID phase area between simulations involving fine-tuned free energy  $F_\theta$  and TDB based free energy  $F_\psi$  is that the a small delay is noticed in melt pool to fully develop when the laser is irradiated at the beginning of the simulation and when the laser is turned off at  $t = 25\text{s}$  there exists a lag in solidification of melt pool phase back to FCC for  $F_\psi$  compared to sharp rise and plummeting of LIQUID phase at the beginning and when laser is turned off for  $F_\theta$ .

based free energy, the three beam profiles of Gaussian, Flat Top and Bessel represented by red, blue, and purple lines in Figure 9(a), (b) and (d) respectively results in similar melt pool area evolution with an average area of  $\approx 15,500 \mu\text{m}^2$ . But for the Ring laser beam denoted by magenta line in

Figure 9(c), the melt pool area is quite lower with an average of  $\approx 12967 \mu\text{m}^2$ .

With the melt pool area versus time plot, we can suggest which beam profile to choose during an additive manufacturing process, for example: for process requiring bigger melt pool and heat affected zone, Flat Top heat source can be utilized which produced the biggest average melt pool size in our simulation ( $16545.82 \mu\text{m}^2$  for  $F_\theta$  and  $15839.72 \mu\text{m}^2$  for  $F_\psi$ ). The relevance of TDB based free energy is more suitable for real experimental comparison as there exists a certain gap between phase and thermal diffusion in real nature which is emulated by the simulation with TDB extracted free energy. Similarly, from the simulations we can infer that for a 3D printing job requiring uniform heating of the material but with a smaller heat affected zone, Ring laser beam profile is more suitable. This analysis paves a way that can help decide the selection of proper laser heat source for specific additive manufacturing task from an equivalent laser processing parameters choices.

An analysis of temperature distribution for four laser beam profile is performed at computational domain's horizontal mid point i.e.  $500 \mu\text{m}$  from left-top edge as marked by a red arrow in a inset picture in Figure 10. The four subplots of Figure 10 shows the thermal history for the entirety of the simulations. In all subplots it can be noticed that the temperature gradually rises, reaches peak when laser source reach the mid-point and then drops afterwards. From Figure 10(a) it is observed that the Gaussian beam produces a higher temperature ( $2873.29 \text{ K}$ ) when the beam centre is just above the domain's midpoint whereas for the Ring beam the system reaches a maximum of  $1975.98 \text{ K}$  when the beam centre move past the midpoint with receding edge of ring shines directly above it at time  $t = 14.46 \text{ s}$  into the simulation. In Figure 10(b) the comparison between temperature distribution from Gaussian and Bessel beam profile is plotted, here we can see that the Gaussian laser beam heats up the domain to a higher temperature than Bessel beam. Similarly, in Figure 10(c), the plot of time-temperature is presented for Ring laser beam versus Flat Top laser beam. In the figure, it can be observed that Flat Top beam profiles causes the domain's top midpoint to heat up to a temperature of  $2843.02 \text{ K}$  at time  $t = 12.5\text{s}$  into the simulation where as an unique flat temperature profile ( $1958.09 \text{ K}$ ) can be seen for Ring laser beam at the midpoint from time  $t = 10.61\text{s}$  to  $14.39\text{s}$ . The flattened temperature profile for Ring beam can be associated with an uniform heating of the domain causing a steady temperature profile when the beam passes through an specific spatial point in the domain with leading and trailing ring edges contributing to the rise in temperature with no irradiance at the beam centre. In case of Figure 10(d), the comparison of temperature distribution due to Flat Top and Bessel laser beam is presented, where it is observed that Flat Top beam imparts more heat energy to the domain with peak temperature greater than that obtained with Bessel beam. In overall, Gaussian, Flat Top and Bessel beam leads to a similar bell shaped temperature profile at a coordinate point on the top surface of the domain whereas for the Ring

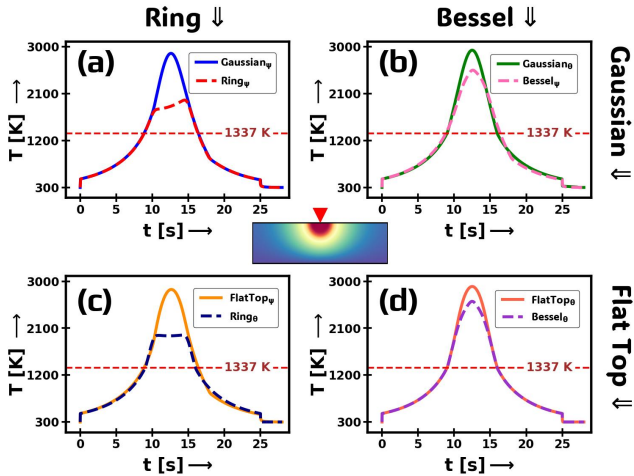


**Figure 10:** The figure illustrates time-temperature plot for a spatial point at the mid-top surface as shown in the inset. The subplot (a) presents the temperature profile for Gaussian and Ring heat sources with  $F_\psi$  denoted by blue solid line and red dashed line respectively. The key observation to be made here is that when the laser passes through the selected point, a bell shaped temperature curve is formed for Gaussian beam with peak reaching to 2873.29 K whereas a flat T-profile is seen for Ring beam peaking around 1975.98 K. In (b) a comparative plot is shown for temperature evolution for Gaussian beam with  $F_\theta$  (green solid line) and Bessel beam with  $F_\psi$  (pink dashed line), it is observed that the Gaussian beam causes the highest temperature rise compared to Bessel beam with a maximum of 2933.98 K compared to 2550.24 K. Similarly, (c) showcases the time-temperature profile for Flat-Top heat source with  $F_\psi$  (yellow solid line) and Ring beam with  $F_\theta$  (dashed blue line). From the plot, it is to be inferred that Ring beam provides an uniform heating where Flat-Top makes the temperature to increase gradually and drop slowly as laser traverses. The peak temperature attained by the point of study for Ring beam with  $F_\theta$  is 1967.24 K and that for Flat-Top with  $F_\psi$  is 2873.02 K. Finally, in (d) the plot showcases the time-temperature profile for Flat-Top laser beam with  $F_\theta$  and Bessel beam with  $F_\psi$  driving force expressions. Both of them generated a similar time-temperature profile with a bell shaped curve reaching to a peak of 2900.08 K and 2614.45 K for Flat-Top and Bessel beam respectively. From the four subplots, it can be noted that to achieve an uniform heating, Ring laser beam is to be preferred compared to other three whereas with a same power and scan speed. Whereas, for processing materials with higher melting point Gaussian or Flat-Top beam is suggested as they produce highly localized and concentrated heating at the beam centre.

beam, an uniform heating scene with flatter peak is observed making it an unique case among four beam shapes studied.

For simulation with fine-tuned free energy expression ( $F_\theta$ ), the effect of laser beam profile on melt pool flow velocity resembles the temperature profile with Gaussian beam inducing the highest flow velocity with an average of  $123.75 \mu\text{m/s}$  denoted by magenta line in Figure 11(a). Whereas, Flat Top laser beam nearly matches the Gaussian beam producing the time-averaged peak flow velocity of  $119.94 \mu\text{m/s}$  depicted by green line in Figure 11(b). For

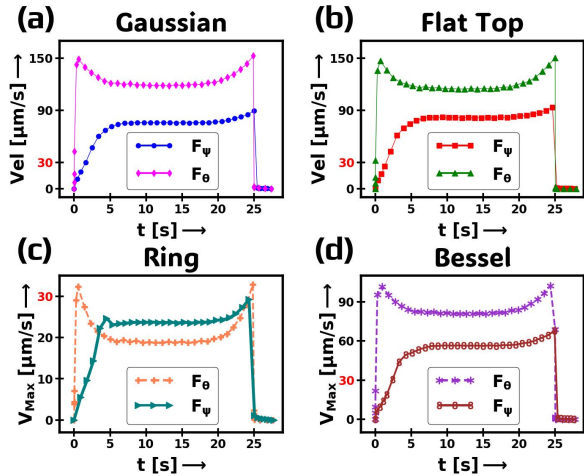


**Figure 11:** Subplots demonstrating maximum flow velocity inside the melt pool over the total duration of simulation with varying laser beam profile and driving free energy expressions. Firstly, in (a) the plot showcases the peak velocity during simulation for both driving force expressions  $F_\theta$  and  $F_\psi$  for Gaussian laser beam. For fine-tuned free energy expression, the peak velocity measured inside the LIQUID phase is higher (magenta line with diamond markers) in-comparison to that with TDB based expression (blue line with circular markers). The average peak velocity in the melt pool over the total duration of simulation for  $F_\theta$  and  $F_\psi$  are  $123.75 \mu\text{m/s}$  and  $71.76 \mu\text{m/s}$  respectively. In a similar trend for Flat-Top laser beam in (b) the velocity inside LIQUID phase in simulation with fine-tuned free energy expression (green line with triangular marker) is higher than  $F_\psi$  (red line with square marker) with an average peak velocity of  $119.94 \mu\text{m/s}$  and  $76.86 \mu\text{m/s}$  respectively. Meanwhile a unique twist is observed for Ring laser heat source results in (c) where the simulation with  $F_\psi$  produced in average a higher flow velocity (cyan line with triangular marker) than that with  $F_\theta$  (orange dashed line with plus marker). The flow inside melt pool over the total simulation duration accounts to an average of  $20.37 \mu\text{m/s}$  for  $F_\theta$  compared to  $22.65 \mu\text{m/s}$  for that of  $F_\psi$ . And for the flow profile with Bessel heat source, the trend follows to that of (a) and (b) but the peak velocity value is relatively lower with an average peak of just  $84.65 \mu\text{m/s}$  (purple dashed line with star marker) and  $52.39 \mu\text{m/s}$  (brown line) for simulations with free energies  $F_\theta$  and  $F_\psi$  respectively. It is to be noted that the y-axis ticks values are different in subplots (c) and (d) to accommodate the range difference, a marker of  $30 \mu\text{m/s}$  is colored in red in all four subplots to make the comparison easier.

the Bessel beam, the aggregate maximum flow velocity over the simulation duration is about  $84.65 \mu\text{m/s}$  represented by purple line in Figure 11(d) and finally, for the Ring beam, the domain-averaged peak flow velocity over time is recorded to be  $20.37 \mu\text{m/s}$ , the lowest among other three beam profiles as presented by cyan coloured line in Figure 11(c). Similarly, for the simulation with TDB based free-energy, the time-averaged maximum flow velocity throughout the simulation period is highest for Flat Top beam followed by Gaussian and Bessel beam and lowest for Ring beam with the values:

$76.86 \mu\text{m/s}$ ,  $71.76 \mu\text{m/s}$ ,  $52.39 \mu\text{m/s}$  and  $22.65 \mu\text{m/s}$  respectively represented by red, blue, brown and orange curves in Figure 11(b), (a), (d) and (c). In a similar fashion to that of temperature profile, for Ring laser beam shape, the peak average velocity is higher for simulation with free energy expression extracted from TDB file ( $F_\psi$ ) compared to that of simulation with fine-tuned free energy expression  $F_\theta$ . The values of which are:  $22.65 \mu\text{m/s}$  and  $20.37 \mu\text{m/s}$  respectively denoted by cyan and orange lines in Figure 11(c).

### 8.3. Machine Learned Meltpool Profiling

The U-Net machine learning architecture model as described in Section 7 was trained for 50 iterations on the dataset generated from the FEM simulations of laser processing. During the 50 epochs, the model peaked an impressive training accuracy of 0.9992 and validation accuracy of 0.9989 by the last iteration. Similarly, the training and validation loss (Binary Cross-Entropy with Logits Loss) were recorded to be 0.0016 and 0.0024 respectively. The training and validation accuracy versus loss plot is presented in Figure 12.

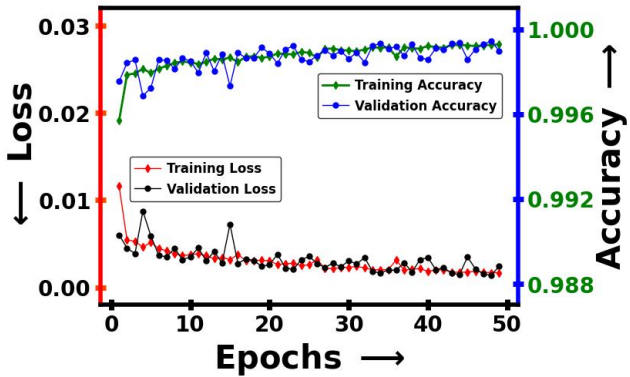


**Figure 12:** The illustration of machine learning model training metrics over the iterations. The model trained for 50 epochs starts with a training and validation loss of around 0.01 at the beginning and gradually the loss metrics is reduced to a minimum of  $1.67 \times 10^{-3}$  and  $2.41 \times 10^{-3}$  represented by red and black lines respectively, corresponding to y-axis at left side of the plot. Whereas, the training and validation accuracy of the model during the training process gradually increased to 0.9993 and 0.9990 by the end of the 50 epoch as shown by green and blue colored lines respectively to the right y-axis in the plot. Following the training and validation metrics, it can be inferred that the model learned absolutely at its best on predicting the phase evolution with input of temperature distribution across the domain.

The trained model is then used to predict the phase for the test-dataset which contained randomly selected 10% of the simulation generated data, these test-dataset were unseen to the model during its training period. The trained model predicted with an average accuracy of 0.9988 for the test-dataset.

$$h_T = \frac{1}{1 + e^{-10\left(\frac{T}{1337} - 1\right)}} \quad (18)$$

To test the actual prediction capabilities of the trained machine learning model, we setup a FEM simulation in MOOSE Framework with just the heat transfer module solving for temperature distribution across the domain under the Bessel laser beam profile with same laser power and scan-speed to the base phase-field simulations. We proceed to introduce an interpolation function as Expresses in Equation 18 that can smoothly switch the material properties such as thermal conductivity, specific heat and density over the domain in relation to the melting temperature of gold (1337 K). The result of FEM simulation without phase field and fluid flow physics was converted to the torch tensor format and was feed to the trained model as an input. The prediction of spatial coordinate of melt pool phase from temperature history data with the trained model was then compared with the phase evolution data generated from phase-field simulation at each time steps of the simulation. Figure 13(a) presents a snapshot of temperature distribution across the domain resulting from the simulation with only heat transfer module active. Whereas, Figure 13(b) shows the phase evolution at the same time point as (a) obtained from the phase-field simulation. Figure 13(c) depicts the phase evolution predicted by the trained machine learning model with the input as temperature distribution of (a) and the error in machine learning model predicted melt pool phase compared to that of phase-field simulation generated result is presented in Figure 13(d). In Figure 13(d) the green color represents the *False Positive* which is the region inside the domain where the ML model predicted the presence of melt pool phase but phase-field simulation result denies any existence of melt pool. Whereas the FN (False Negative) region in red color means the ML model could not predict the LIQUID phase at those spatial points where the phase-field simulation result suggests there should be LIQUID phase. The coordinate space where both the phase-field simulation result and ML model predicted result align with each other is marked as Correctly Predicted (CP) region shown in light-yellow color. A video animation comparing the of results phase evolution generated from phase-field simulation and ML predicted at every time step of laser simulation is provided in Section 13 as well as in Appendix B.

## 9. Virtual Digital Twin and Future Work

Virtual Digital twin [69]

With the trained machine learning model, we propose for the construction of Digital Twin which aids in quantifying and predict the phase evolution, velocity profile and other material properties on real time during an additive manufacturing processes such as laser 3D printing. For this, the trained ML model can be operated from a minicomputer device as *Raspberry Pi* with an Infra-Red camera module that can feed the temperature data of the experimental specimen surface to the model and the model displays the detail information related to phase transformation on a portable monitor on real time. For the conceptualization of such digital twin, we constructed

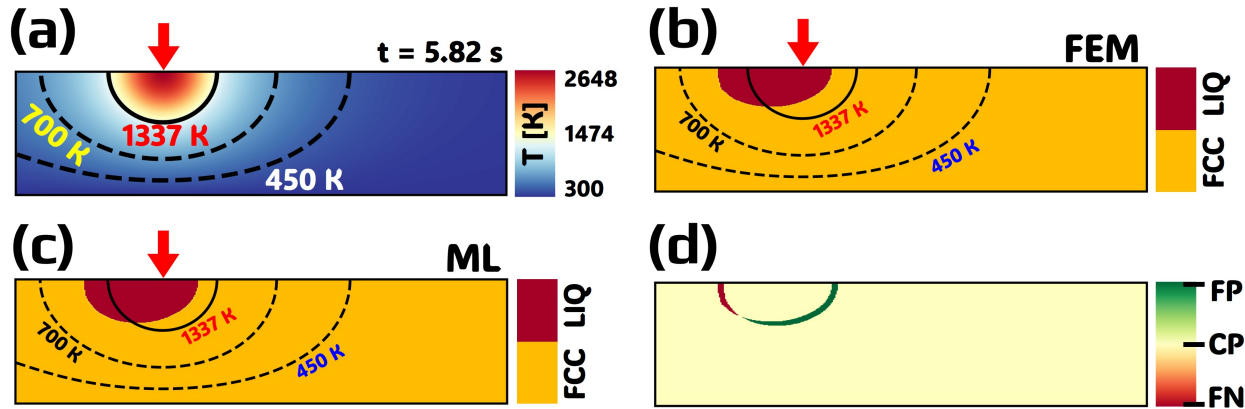


**Figure 13:** A snapshot of test demo for the result of prediction made by the trained machine learning model compared to the phase evolution computed from FEM simulation with the error and accuracy in predicted phase. **(a)** The input supplied to the trained ML model with the data of temperature distribution across the domain, the temperature history is computed via a laser heat transfer simulation without phase field module. In a real-time Digital Twin model prediction scenario, the temperature distribution as an input to the ML model is supplied from the IR camera with a post-processing performed to match the model input shape in micro-computer as *Raspberry Pi*. **(b)** The phase evolution data computed from the phase field modelling of laser processing simulated via FEM with the exactly same laser processing parameters to that of **(a)** presented at the same time instance of  $t=5.82\text{ s}$  into the simulation. In **(c)**, the predicted result of two phases LIQUID and FCC from the trained ML model with an input of temperature distribution **(a)**. Finally in **(d)**, the comparison between phase field simulation computed result of phase evolution in **(b)** and machine learning model predicted of phase evolution of **(c)** with just the thermal distribution data of **(a)**. The three colors inside the domain represent three different regions comparing the results of **(b)** and **(c)** with light yellow color denoted by CP meaning the *Correct Prediction* from ML model with respect to phase field generated result, green color region represented by FP denote to the *False Positive* indicating that the presence of phase was predicted by the ML model but phase field simulation suggests that there is actually absence of the respective phase. Finally the red colored region marked by FN stands for *False Negative* suggesting that the machine learning model failed to predict the presence of a phase which is calculated via phase field simulation. Overall, it can be noted that the majority of the region inside the domain is correctly predicted by the ML model with irregularities at the interface of LIQUID and FCC phase, and the prediction accuracy can be further increased in those interfaces with a stronger ML model trained with multiple more simulation data for a longer training iterations in further work.

a demo WebApp where user can upload the temperature data (in numpy format) and the ML model provides a 2D image of meltpool and solid phase as output. The WebApp is available at : [https://github.com/subediupadेश/Digital\\_Additive\\_Manufacturing/tree/main/6\\_Machine\\_Learning](https://github.com/subediupadेश/Digital_Additive_Manufacturing/tree/main/6_Machine_Learning). The Machine Learning model's prediction scope will be further enhance and broaden in future work by incorporating the training data of laser processing of multiple materials (multi-component alloys) at different length scale with varying laser parameters (power and scan-speed) making a multi-material Digital Twin model.

### 9.1. Image Model

### 9.2. Spatio Temporal Intelligent Model

### 9.3. Technology Readiness Level

Remote operation of micro-computer Raspberry Pi, with wireless technology such as: Wifi, Mouse, Keyboard, Connect Raspberry Pi, Remote shell, Hazardous environment Physics Informed Virtual Digital Twin

## 10. Conclusion

In this study we presented the result of computational modelling of laser induced phase transformation and microstructural evolution in unary Au system. Multiple simulations were performed by varying laser beam profiles of Gaussian, Flat-Top, Ring and Bessel types, along with multiple different free energy expressions driving the phase transition phenomenon. The free energy expression in consideration were higher order logarithmic-polynomial fitted expression and expression extracted from Thermodynamic Data Base file. The phase transformation due to heat deposition from different laser types were typically similar in nature for Gaussian, Flat-Top and Bessel beam with maximum temperature measured at the beam centre and radially distributed outwards, similar is the case for flow velocity inside meltpool where the maximum velocity profile is observed at the centre of beam. A drastic different result was noticed for Ring beam profile where the thermal distribution was observed to be uniform inside the ring beam radius. The most intriguing distinction was found in phase evolution with the variation of driving force expressions. For the fine-tuned (fitted) expression, it was observed that the melting point of Au dictated the LIQUID phase exactly matching the

temperature contour of 1337 K as the interface of FCC and LIQUID phases whereas a unique phenomenon of thermal front leading the phase front was noticed in simulations conducted under TDB extracted free energy expressions. For the TDB based driving force, the lead-lag dynamics of phase and thermal front was concluded to be linked with the thermal and phase diffusion rates differing with each other making it more realistic according to the thermodynamics. Finally, a U-Net machine learning model architecture was trained on the simulation dataset of thermal history correlating with the meltpool phase evolution. With the trained model a prediction framework is developed where user can interact with the model by uploading the T-data not only from simulation but also from experimental results in a 2D array format. This framework can be regarded as a first step towards the construction of a Digital Twin capable of predicting phase evolution in real time experiments with input data taken from infrared cameras onsite. Currently, the model is limited to a single component Au system which will be expanded to multi-component alloy system in a multitude of laser processing parameters in future studies. The development of multimodal Digital Twin is expected to expedite the real-time prediction of phase transformation, and details related to evolving phases making it as milestone in precision engineering in Additive Manufacturing sector.

## 11. Declarations

The authors declare to have no conflicts of interest that are relevant to the content of this article.

## 12. Acknowledgment

This work was supported by the National Science Centre, Poland (UMO-2021/42/E/ST5/00339).

## 13. Data Availability

Codes and data used for this work is available at [https://github.com/subediupadeth/Digital\\_Additive\\_Manufacturing](https://github.com/subediupadeth/Digital_Additive_Manufacturing).

## CRediT authorship contribution statement

**Upadeth Subedi:** Conceptualization, Methodology, Software, Validation, Formal analysis, Investigation, Data Curation, Writing - Original Draft, Visualization. **Nele Moelans:** Methodology, Validation, Writing - Review & Editing, Supervision. **Tomasz Tański:** Validation, Visualization, Writing - Review & Editing, Supervision. **Anil Kunwar:** Conceptualization, Methodology, Validation, Data Curation, Supervision, Writing - Review & Editing, Project administration, Funding acquisition.

## References

- [1] N. M. Tripathi, A. Sharma, *Advances in Pre- and Post-Additive Manufacturing Processes*, CRC Press, Boca Raton, 2024. doi:[10.1201/9781003428862](https://doi.org/10.1201/9781003428862). URL <https://www.taylorfrancis.com/books/9781003428862>
- [2] J. An, B. Li, *Application and Comparison of Additive Manufacturing Technology in Rocket Manufacturing*, Highlights in Science, Engineering and Technology 76 (2023) 296–307. doi:[10.54097/4r1k0e19](https://doi.org/10.54097/4r1k0e19). URL <https://drpress.org/ojs/index.php/HSET/article/view/15933>
- [3] L. Zhang, J. Lu, E. Takashi, S. Matsumoto, *Rapid Manufacturing Approach of an Ultrathin Moisture Sensor for Health Monitoring*, Sensors 23 (9) (2023) 4262. doi:[10.3390/s23094262](https://doi.org/10.3390/s23094262). URL <https://www.mdpi.com/1424-8220/23/9/4262>
- [4] R. de Freitas Bart, *Is Hardware Agile Worth It? - Analyzing the SpaceX Development Process*, in: AIAA SCITECH 2024 Forum, American Institute of Aeronautics and Astronautics, Reston, Virginia, 2024. doi:[10.2514/6.2024-2054](https://doi.org/10.2514/6.2024-2054). URL <https://arc.aiaa.org/doi/10.2514/6.2024-2054>
- [5] N. Bastola, M. P. Jahan, N. Rangasamy, C. S. Rakurty, *A Review of the Residual Stress Generation in Metal Additive Manufacturing: Analysis of Cause, Measurement, Effects, and Prevention*, Micromachines 14 (7) (2023) 1480. doi:[10.3390/mi14071480](https://doi.org/10.3390/mi14071480). URL <https://www.mdpi.com/2072-666X/14/7/1480>
- [6] H. Zhao, C. Yu, Z. Liu, C. Liu, Y. Zhan, *A novel finite element method for simulating residual stress of TC4 alloy produced by laser additive manufacturing*, Optics & Laser Technology 157 (2023) 108765. doi:[10.1016/j.optlastec.2022.108765](https://doi.org/10.1016/j.optlastec.2022.108765). URL <https://linkinghub.elsevier.com/retrieve/pii/S0030399222009112>
- [7] M. R. Tonks, A. Cheniour, L. Aagesen, *How to apply the phase field method to model radiation damage*, Computational Materials Science 147 (2018) 353–362. doi:[10.1016/j.commatsci.2018.02.007](https://doi.org/10.1016/j.commatsci.2018.02.007).
- [8] J.-O. Andersson, T. Helander, L. Höglund, P. Shi, B. Sundman, *Thermo-Calc & DICTRA, computational tools for materials science*, Calphad 26 (2) (2002) 273–312. doi:[10.1016/S0364-5916\(02\)00037-8](https://doi.org/10.1016/S0364-5916(02)00037-8). URL <https://linkinghub.elsevier.com/retrieve/pii/S0364591602000378>
- [9] R. Darabi, E. Azinpour, A. Reis, J. C. de Sa, *Multi-scale Multi-physics Phase-field coupled Thermo-mechanical approach for modeling of powder bed fusion process*, Applied Mathematical Modelling 122 (2023) 572–597. doi:[10.1016/j.apm.2023.06.021](https://doi.org/10.1016/j.apm.2023.06.021). URL <https://linkinghub.elsevier.com/retrieve/pii/S0307904X23002767>
- [10] D. Gaston, C. Newman, G. Hansen, D. Lebrun-Grandié, *Moose: A parallel computational framework for coupled systems of nonlinear equations*, Nuclear Engineering and Design 239 (2009) 1768–1778. doi:[10.1016/j.nucengdes.2009.05.021](https://doi.org/10.1016/j.nucengdes.2009.05.021). URL <https://linkinghub.elsevier.com/retrieve/pii/S0029549309002635>
- [11] A. D. Lindsay, D. R. Gaston, C. J. Permann, J. M. Miller, D. Andrš, A. E. Slaughter, F. Kong, J. Hansel, R. W. Carlsen, C. Icenhour, L. Harbour, G. L. Giudicelli, R. H. Stogner, P. German, J. Badger, S. Biswas, L. Chapuis, C. Green, J. Hales, T. Hu, W. Jiang, Y. S. Jung, C. Matthews, Y. Miao, A. Novak, J. W. Peterson, Z. M. Prince, A. Rovinelli, S. Schunert, D. Schwen, B. W. Spencer, S. Veeraraghavan, A. Recuero, D. Yushu, Y. Wang, A. Wilkins, C. Wong, *2.0 - moose: Enabling massively parallel multiphysics simulation*, SoftwareX 20 (2022) 101202. doi:[10.1016/j.softx.2022.101202](https://doi.org/10.1016/j.softx.2022.101202). URL <https://linkinghub.elsevier.com/retrieve/pii/S2352711022001200>
- [12] Z. Li, M. Greenwood, A. Phillion, *A phase field methodology for simulating the microstructure evolution during laser powder bed fusion in-situ alloying process*, IOP Conference Series: Materials Science and Engineering 1281 (1) (2023) 012017. doi:[10.1088/1757-899X/1281/1/012017](https://doi.org/10.1088/1757-899X/1281/1/012017). URL <https://iopscience.iop.org/article/10.1088/1757-899X/1281/1/012017>
- [13] O. Ronneberger, P. Fischer, T. Brox, *U-Net: Convolutional Networks for Biomedical Image Segmentation*, 2015, pp. 234–241. doi:[10.1007/978-3-319-24574-4\\_28](https://doi.org/10.1007/978-3-319-24574-4_28).
- [14] A. Kunwar, B. Guo, S. Shang, P. Råback, Y. Wang, J. Chen, H. Ma, X. Song, N. Zhao, *Roles of interfacial heat transfer and relative solder*

- height on segregated growth behavior of intermetallic compounds in sn/cu joints during furnace cooling, *Intermetallics* 93 (2018) 186–196. doi:[10.1016/j.intermet.2017.11.021](https://doi.org/10.1016/j.intermet.2017.11.021).
- [15] S. Chen, A. Lu, D. Yang, S. Lu, J. Dong, C. Dong, Analysis on flow pattern of bobbin tool friction stir welding for 6082 aluminum, Elsevier, 2013, pp. 353–358. doi:[10.1533/978-1-78242-164-1.353](https://doi.org/10.1533/978-1-78242-164-1.353).
- [16] N. Moelans, **A quantitative and thermodynamically consistent phase-field interpolation function for multi-phase systems**, *Acta Materialia* 59 (2011) 1077–1086. doi:[10.1016/j.actamat.2010.10.038](https://doi.org/10.1016/j.actamat.2010.10.038).  
URL <https://linkinghub.elsevier.com/retrieve/pii/S1359645410007019>
- [17] H. B. Mamo, U. Subedi, T. Poloczek, M. Adamiak, A. N. S. Appiah, M. Skonieczna, P. M. Nuckowski, Y. Geng, B. Haldar, A. Kunwar, Prototyping ti2cu intermetallic grain growth heterogeneously in ti6al4v matrix through laser additive manufacturing, *Materials & Design* 246 (2024) 113312. doi:[10.1016/j.matdes.2024.113312](https://doi.org/10.1016/j.matdes.2024.113312).
- [18] U. Subedi, N. Moelans, T. Tański, A. Kunwar, **Tracking meltpool dynamics and interfacial intermetallic grains in laser-processed ti-ai system: A non-isothermal phase field approach.**, Journal Name 000000 (2024) 000000. doi:[00.0000/j.000000.2024.000000](https://doi.org/10.1016/j.matdes.2024.113312).  
URL <https://linkinghub.elsevier.com/retrieve/pii/S000000000000>
- [19] C. N. Singman, **Atomic volume and allotropy of the elements**, *Journal of Chemical Education* 61 (1984) 137–142. doi:[10.1021/ed061p137](https://doi.org/10.1021/ed061p137).  
URL <https://pubs.acs.org/doi/abs/10.1021/ed061p137>
- [20] A. Kunwar, E. Yousefi, X. Zuo, Y. Sun, D. Seveno, M. Guo, N. Moelans, **Multi-phase field simulation of Al3Ni2 intermetallic growth at liquid Al/solid Ni interface using MD computed interfacial energies**, *International Journal of Mechanical Sciences* 215 (2022) 106930. doi:[10.1016/j.ijmecsci.2021.106930](https://doi.org/10.1016/j.ijmecsci.2021.106930).  
URL <https://linkinghub.elsevier.com/retrieve/pii/S0020740321006408>
- [21] S. Poudel, N. Moelans, R. Thapa, A. Timofiejczuk, D. Panthi, A. Kunwar, **Unraveling elastochemical effects in microstructural evolution of Al–Cu–Ni system through DFT-informed multi-phase field simulations**, *International Journal of Solids and Structures* 300 (2024) 112894. doi:[10.1016/j.ijsolstr.2024.112894](https://doi.org/10.1016/j.ijsolstr.2024.112894).  
URL <https://linkinghub.elsevier.com/retrieve/pii/S0020768324002531>
- [22] H. Verbeeck, V. Feyen, I. Bellemans, N. Moelans, **Multi-phase-field modeling of the dissolution behavior of stoichiometric particles on experimentally relevant length scales**, *Computational Materials Science* 245 (2024) 113288. doi:[10.1016/j.commatsci.2024.113288](https://doi.org/10.1016/j.commatsci.2024.113288).  
URL <https://linkinghub.elsevier.com/retrieve/pii/S0927025624005093>
- [23] F. Jing, Y. Liu, Y. Du, C. Shi, B. Hu, X. He, Phase equilibria, thermodynamics and solidified microstructure in the copper-zirconium-yttrium system, *Materials* 16 (2023) 2063. doi:[10.3390/ma16052063](https://doi.org/10.3390/ma16052063).
- [24] A. Dinsdale, Sgte data for pure elements, *Calphad* 15 (1991) 317–425. doi:[10.1016/0364-5916\(91\)90030-N](https://doi.org/10.1016/0364-5916(91)90030-N).
- [25] A. Khvan, I. Uspenskaya, N. Aristova, Q. Chen, G. Trimarchi, N. Konstantinova, A. Dinsdale, **Description of the thermodynamic properties of pure gold in the solid and liquid states from 0 K**, *Calphad* 68 (2020) 101724. doi:[10.1016/j.calphad.2019.101724](https://doi.org/10.1016/j.calphad.2019.101724).  
URL <https://linkinghub.elsevier.com/retrieve/pii/S0364591619302858>
- [26] B. Echebarria, R. Folch, A. Karma, M. Plapp, **Quantitative phase-field model of alloy solidification**, *Physical Review E* 70 (6) (2004) 061604. doi:[10.1103/PhysRevE.70.061604](https://doi.org/10.1103/PhysRevE.70.061604).  
URL <https://link.aps.org/doi/10.1103/PhysRevE.70.061604>
- [27] T. Uehara, M. Fukui, N. Ohno, **Phase field simulations of stress distributions in solidification structures**, *Journal of Crystal Growth* 310 (7-9) (2008) 1331–1336. doi:[10.1016/j.jcrysGro.2007.12.035](https://doi.org/10.1016/j.jcrysGro.2007.12.035).  
URL <https://linkinghub.elsevier.com/retrieve/pii/S0022024807012109>
- [28] X. Feng, A. Prohl, **Analysis of a fully discrete finite element method for the phase field model and approximation of its sharp interface limits**, *Mathematics of Computation* 73 (246) (2003) 541–567. doi:[10.1090/S0025-5718-03-01588-6](https://doi.org/10.1090/S0025-5718-03-01588-6).
- [29] U. Subedi, **tumbleweed - a moose framework based application** (2023).  
URL <https://github.com/subediupadeth/tumbleweed>
- [30] U. Subedi, **Free energy benchmark model** (2024).  
URL [https://github.com/subediupadeth/FreeEnergy\\_Benchmark\\_Model](https://github.com/subediupadeth/FreeEnergy_Benchmark_Model)
- [31] S. A. Khairallah, A. T. Anderson, A. Rubenchik, W. E. King, **Laser powder-bed fusion additive manufacturing: Physics of complex melt flow and formation mechanisms of pores, spatter, and denudation zones**, *Acta Materialia* 108 (2016) 36–45. doi:[10.1016/j.actamat.2016.02.014](https://doi.org/10.1016/j.actamat.2016.02.014).
- [32] Y.-C. Wu, C.-H. San, C.-H. Chang, H.-J. Lin, R. Marwan, S. Baba, W.-S. Hwang, **Numerical modeling of melt-pool behavior in selective laser melting with random powder distribution and experimental validation**, *Journal of Materials Processing Technology* 254 (2018) 72–78. doi:[10.1016/j.jmatprotec.2017.11.032](https://doi.org/10.1016/j.jmatprotec.2017.11.032).  
URL <https://linkinghub.elsevier.com/retrieve/pii/S0924013617305526>
- [33] A. Kunwar, S. Shang, P. Råback, Y. Wang, J. Givernaud, J. Chen, H. Ma, X. Song, N. Zhao, **Heat and mass transfer effects of laser soldering on growth behavior of interfacial intermetallic compounds in Sn/Cu and Sn-3.5Ag0.5/Cu joints**, *Microelectronics Reliability* 80 (2018) 55–67. doi:<https://doi.org/10.1016/j.microrel.2017.11.016>.  
URL <https://www.sciencedirect.com/science/article/pii/S0026271417305449>
- [34] R. Moore, G. Orlandi, T. Rodgers, D. Moser, H. Murdoch, F. Abdelljawad, **Microstructure-Based Modeling of Laser Beam Shaping During Additive Manufacturing**, *Jom* 76 (3) (2024) 1726–1736. doi:[10.1007/s11837-023-06363-8](https://doi.org/10.1007/s11837-023-06363-8).  
URL <https://link.springer.com/10.1007/s11837-023-06363-8>
- [35] C. Wang, Z. Luo, J. Duan, L. Jiang, X. Sun, Y. Hu, J. Zhou, Y. Lu, **Adjustable annular rings of periodic surface structures induced by spatially shaped femtosecond laser**, *Laser Physics Letters* 12 (5) (2015) 056001. doi:[10.1088/1612-2011/12/5/056001](https://doi.org/10.1088/1612-2011/12/5/056001).  
URL <https://iopscience.iop.org/article/10.1088/1612-2011/12/5/056001>
- [36] C. Lei, S. Ren, C. Yin, X. Liu, M. Chen, J. Wu, C. Han, **Manipulating melt pool thermofluidic transport in directed energy deposition driven by a laser intensity spatial shaping strategy**, *Virtual and Physical Prototyping* 19 (1) (dec 2024). doi:[10.1080/17452759.2024.2308513](https://doi.org/10.1080/17452759.2024.2308513).  
URL <https://www.tandfonline.com/doi/full/10.1080/17452759.2024.2308513>
- [37] F. Galbusera, L. Caprio, B. Previtali, A. G. Demir, **Analytical modeling and characterization of ring beam profiles for high-power lasers used in industrial manufacturing**, *Journal of Manufacturing Processes* 117 (2024) 387–404. doi:[10.1016/j.jmapro.2024.02.069](https://doi.org/10.1016/j.jmapro.2024.02.069).  
URL <https://linkinghub.elsevier.com/retrieve/pii/S1526612524002093>
- [38] T. M. Wischeropp, H. Tarhini, C. Emmelmann, **Influence of laser beam profile on the selective laser melting process of als10mg**, *Journal of Laser Applications* 32 (5 2020). doi:[10.2351/7.0000100](https://doi.org/10.2351/7.0000100).
- [39] T. U. Tumkur, T. Voisin, R. Shi, P. J. Depond, T. T. Roehling, S. Wu, M. F. Crumb, J. D. Roehling, G. Guss, S. A. Khairallah, M. J. Matthews, **Nondiffractive beam shaping for enhanced optothermal control in metal additive manufacturing**, *Science Advances* 7 (9 2021). doi:[10.1126/sciadv.abg9358](https://doi.org/10.1126/sciadv.abg9358).
- [40] L.-E. Loh, C.-K. Chua, W.-Y. Yeong, J. Song, M. Mapar, S.-L. Sing, Z.-H. Liu, D.-Q. Zhang, **Numerical investigation and an effective modelling on the Selective Laser Melting (SLM) process with aluminium alloy 6061**, *International Journal of Heat and Mass Transfer* 80 (2015) 288–300. doi:[10.1016/j.ijheatmasstransfer.2014.09.014](https://doi.org/10.1016/j.ijheatmasstransfer.2014.09.014).  
URL <https://linkinghub.elsevier.com/retrieve/pii/S0020740314008060>
- [41] S. Chowdhury, N. Yadaiah, C. Prakash, S. Ramakrishna, S. Dixit, L. R. Gupta, D. Buddhi, **Laser powder bed fusion: a state-of-the-art review of the technology, materials, properties & defects, and**

- numerical modelling, Journal of Materials Research and Technology 20 (2022) 2109–2172. doi:10.1016/j.jmrt.2022.07.121.
- URL <https://linkinghub.elsevier.com/retrieve/pii/S2238785422011607>
- [42] T. Kik, Heat Source Models in Numerical Simulations of Laser Welding, Materials 13 (11) (2020) 2653. doi:10.3390/ma13112653.
- URL <https://www.mdpi.com/1996-1944/13/11/2653>
- [43] H. Yang, Z. Li, S. Wang, The Analytical Prediction of Thermal Distribution and Defect Generation of Inconel 718 by Selective Laser Melting, Applied Sciences 10 (20) (2020) 7300. doi:10.3390/app10207300.
- URL <https://www.mdpi.com/2076-3417/10/20/7300>
- [44] E. Mirkoohi, D. E. Sievers, H. Garmestani, S. Y. Liang, Thermo-mechanical modeling of thermal stress in metal additive manufacturing considering elastoplastic hardening, CIRP Journal of Manufacturing Science and Technology 28 (2020) 52–67. doi:10.1016/j.cirpj.2020.01.002.
- [45] J. Singh, J. Oliveira, H. Taylor, J. Mireles, R. Wicker, A holistic approach for evaluation of Gaussian versus ring beam processing on structure and properties in laser powder bed fusion, Journal of Materials Processing Technology 325 (2024) 118293. doi:10.1016/j.jmatprotec.2024.118293.
- URL <https://linkinghub.elsevier.com/retrieve/pii/S0924013624000116>
- [46] Y.-N. Liu, E. Kannatey-Asibu, Laser Beam Welding With Simultaneous Gaussian Laser Preheating, Journal of Heat Transfer 115 (1) (1993) 34–41. doi:10.1115/1.2910666.
- URL <https://asmedigitalcollection.asme.org/heattransfer/article/115/1/34/412942/>
- [47] G. Caprino, V. Tagliaferri, L. Covelli, Cutting glass fibre reinforced composites using CO<sub>2</sub> laser with multimodal-Gaussian distribution, International Journal of Machine Tools and Manufacture 35 (6) (1995) 831–840. doi:10.1016/0890-6955(94)00054-N.
- URL <https://linkinghub.elsevier.com/retrieve/pii/089069559400054N>
- [48] S. C. Holswade, F. M. Dickey, Gaussian laser beam shaping: test and evaluation, in: R. E. Fischer, W. J. Smith (Eds.), Current Developments in Optical Design and Engineering VI, Vol. 2863, International Society for Optics and Photonics, SPIE, 1996, pp. 237 – 245. doi:10.1117/12.256229.
- URL <https://doi.org/10.1117/12.256229>
- [49] J. Wu, H. Wei, F. Yuan, P. Zhao, Y. Zhang, Effect of beam profile on heat and mass transfer in filler powder laser welding, Journal of Materials Processing Technology 258 (2018) 47–57. doi:10.1016/j.jmatprotec.2018.03.011.
- URL <https://linkinghub.elsevier.com/retrieve/pii/S092401361830116X>
- [50] D. E. Jodi, T. Kitashima, Y. Koizumi, T. Nakano, M. Watanabe, Manufacturing single crystals of pure nickel via selective laser melting with a flat-top laser beam, Additive Manufacturing Letters 3 (2022) 100066. doi:10.1016/j.addlet.2022.100066.
- URL <https://linkinghub.elsevier.com/retrieve/pii/S2772369022000408>
- [51] W. Jiazhu, T. Liu, H. Chen, F. Li, H. Wei, Y. Zhang, Simulation of laser attenuation and heat transport during direct metal deposition considering beam profile, Journal of Materials Processing Technology 270 (2019) 92–105. doi:10.1016/j.jmatprotec.2019.02.021.
- URL <https://linkinghub.elsevier.com/retrieve/pii/S0924013619300779>
- [52] D. L. Shealy, J. A. Hoffnagle, Laser beam shaping profiles and propagation, Applied Optics 45 (21) (2006) 5118. doi:10.1364/AO.45.005118.
- URL <https://opg.optica.org/abstract.cfm?URI=ao-45-21-5118>
- [53] Z. Wang, M. Jiang, X. Chen, Y. Du, Z. Lei, S. Zhao, Y. Chen, Mitigating spatters in keyhole-mode laser welding by superimposing additional ring-shaped beam, Optics & Laser Technology 168 (2024) 109869. doi:10.1016/j.optlastec.2023.109869.
- URL <https://linkinghub.elsevier.com/retrieve/pii/S0030399223007624>
- [54] L. Yang, S. Geng, P. Jiang, Y. Wang, J. Xiong, Investigation on the keyhole/molten pool dynamic behavior during adjustable ring-mode laser welding of medium-thick aluminum alloy, International Journal of Thermal Sciences 196 (2024) 108723. doi:10.1016/j.ijthermalsci.2023.108723.
- URL <https://linkinghub.elsevier.com/retrieve/pii/S1290072923005847>
- [55] I. Abdo, N. Ashry, M. Sadek, M. Abdel Hakim, D. Khalil, Effect of ring width on ring generated Bessel beam, 2012, p. 823608. doi:10.1117/12.908956.
- URL <http://proceedings.spiedigitallibrary.org/proceeding.aspx?doi=10.1117/12.908956>
- [56] P. Pradhan, M. Sharma, B. Ung, Generation of Perfect Cylindrical Vector Beams With Complete Control Over the Ring Width and Ring Diameter, IEEE Photonics Journal 10 (1) (2018) 1–10. doi:10.1109/JPHOT.2018.2790175.
- URL <https://ieeexplore.ieee.org/document/8252695/>
- [57] A. Zapata, X. F. Zhao, S. Li, C. Bernauer, M. F. Zaeh, Three-dimensional annular heat source for the thermal simulation of coaxial laser metal deposition with wire, Journal of Laser Applications 35 (1) (feb 2023). doi:10.2351/7.0000813.
- URL <https://pubs.aip.org/jla/article/35/1/012020/2871665/Three-dimensional-annular-heat-source-for-the>
- [58] M. Duocastella, C. Arnold, Bessel and annular beams for materials processing, Laser & Photonics Reviews 6 (5) (2012) 607–621. doi:10.1002/lpor.201100031.
- URL <https://onlinelibrary.wiley.com/doi/10.1002/lpor.201100031>
- [59] G. S. Sokolovskii, V. V. Dudelev, S. N. Losev, K. K. Soboleva, A. G. Deryagin, K. A. Fedorova, V. I. Kuchinskii, W. Sibbett, E. U. Rafailov, Bessel beams from semiconductor light sources, Progress in Quantum Electronics 38 (2014) 157–188. doi:10.1016/J.PQUANTELEC.2014.07.001.
- [60] O. Bialas, A. N. Appiah, M. Wala, A. Kunwar, A. Woźniak, P. M. Nuckowski, W. Simka, P. Räback, M. Adamiak, Laser assisted fabrication of mechanochemically robust Ti3Au intermetallic at Au-Ti interface, Engineering Science and Technology, an International Journal 42 (2023) 101413. doi:10.1016/j.jestch.2023.101413.
- URL <https://linkinghub.elsevier.com/retrieve/pii/S2215098623000903>
- [61] W. Luo, Z. Jin, H. Liu, T. Wang, Thermodynamic assessment of the au-ti system, Calphad 25 (2001) 19–26. doi:10.1016/S0364-5916(01)00026-8.
- [62] T. Dubberstein, M. Schürmann, H. Chaves, H. P. Heller, C. G. Aneziris, A novel vibrating finger viscometer for high-temperature measurements in liquid metals and alloys, International Journal of Thermophysics 37 (2016) 100. doi:10.1007/s10765-016-2104-7.
- URL <http://link.springer.com/10.1007/s10765-016-2104-7>
- [63] P. Nath, Z. Hu, S. Mahadevan, Uncertainty quantification of grain morphology in laser direct metal deposition, Modelling and Simulation in Materials Science and Engineering 27 (4) (2019) 044003. doi:10.1088/1361-651X/ab1676.
- URL <https://iopscience.iop.org/article/10.1088/1361-651X/ab1676>
- [64] Z. Hu, S. Mahadevan, Uncertainty quantification and management in additive manufacturing: current status, needs, and opportunities, The International Journal of Advanced Manufacturing Technology 93 (5–8) (2017) 2855–2874. doi:10.1007/s00170-017-0703-5.
- URL <http://link.springer.com/10.1007/s00170-017-0703-5>
- [65] Z. Hu, S. Mahadevan, Uncertainty quantification in prediction of material properties during additive manufacturing, Scripta Materialia 135 (2017) 135–140. doi:10.1016/j.scriptamat.2016.10.014.
- URL <https://linkinghub.elsevier.com/retrieve/pii/S1359646216305097>
- [66] Siemens, A comprehensive Digital Twin (2023).
- URL <https://www.siemens.com/global/en/products/automation/topic-areas/digital-enterprise/digital-twin.html>

- [67] Raspberry Pi, We are Raspberry Pi. We make computers.  
URL <https://www.raspberrypi.com/about/>
- [68] C. R. Harris, K. J. Millman, S. J. van der Walt, R. Gommers, P. Virtanen, D. Cournapeau, E. Wieser, J. Taylor, S. Berg, N. J. Smith, R. Kern, M. Picus, S. Hoyer, M. H. van Kerkwijk, M. Brett, A. Haldane, J. F. del Río, M. Wiebe, P. Peterson, P. Gérard-Marchant, K. Sheppard, T. Reddy, W. Weckesser, H. Abbasi, C. Gohlke, T. E. Oliphant, Array programming with NumPy, Nature 585 (7825) (2020) 357–362. doi:10.1038/s41586-020-2649-2.  
URL <https://doi.org/10.1038/s41586-020-2649-2>
- [69] M. Rezasefat, J. D. Hogan, Virtual rapid prototyping of materials with deep learning: spatiotemporal stress fields prediction in ceramics employing convolutional neural networks and transfer learning, Virtual and Physical Prototyping 19 (12) 2024. doi:10.1080/17452759.2024.2399186.

## Appendix A:

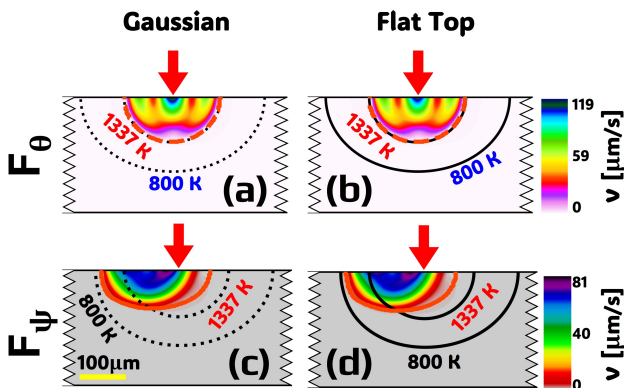


**Figure A1:** The illustration of velocity profile inside the melt pool when the laser heat source traverses to the domain midpoint at 12.5s into the simulation. Subplot (a) and (c) are associated with simulation under the Gaussian heat source for free energy expression of  $F_\theta$  and  $F_\psi$  respectively. The peak flow velocity for in the LIQUID phase for (a) and (c) are 119  $\mu\text{m}/\text{s}$  and 75.61  $\mu\text{m}/\text{s}$  respectively. In (b) and (d), the flow profile for simulation conducted under the Flat-Top heat source for  $F_\theta$  and  $F_\psi$  is presented. Although visually the velocity profile between results from Gaussian and Flat-Top laser beam look alike there exists a smaller difference in numerical value of peak melt pool flow velocity reached at the illustrated time stamp with 114.47  $\mu\text{m}/\text{s}$  and 81  $\mu\text{m}/\text{s}$  for Flat-Top laser induced flow for  $F_\theta$  and  $F_\psi$  respectively.

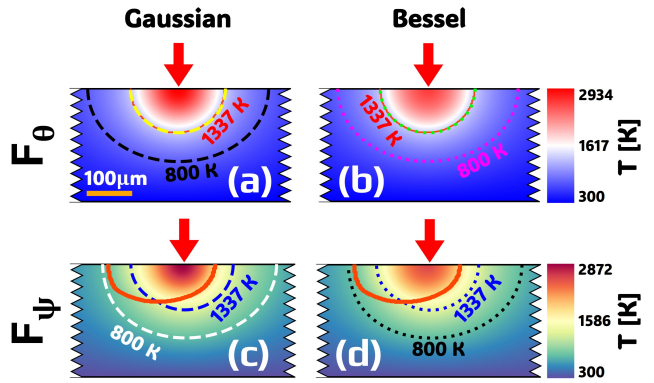


**Figure A2:** Visualization of thermal distribution across a cutout of simulation domain for Gaussian and Bessel laser sources. Plot (a) and (c) showcases the temperature profile for Gaussian heat source with driving force expression of  $F_\theta$  and  $F_\psi$  respectively. Similarly, (b) and (d) represents the temperature inside the computational domain with Bessel heat source for  $F_\theta$  and  $F_\psi$  correspondingly. A subtle difference in temperature profile can be noticed between Gaussian and Bessel based simulation results with a higher concentration of temperature distribution at the beam centre for Gaussian beam, the peak temperature reached by the domain under Bessel beam are found to be 2613.11 K in (b) and 2548.95 K in (d).

## Appendix B:

### Video Animations:

Video Animation of Phase-evolution comparison between ML predicted and phase-field generated:

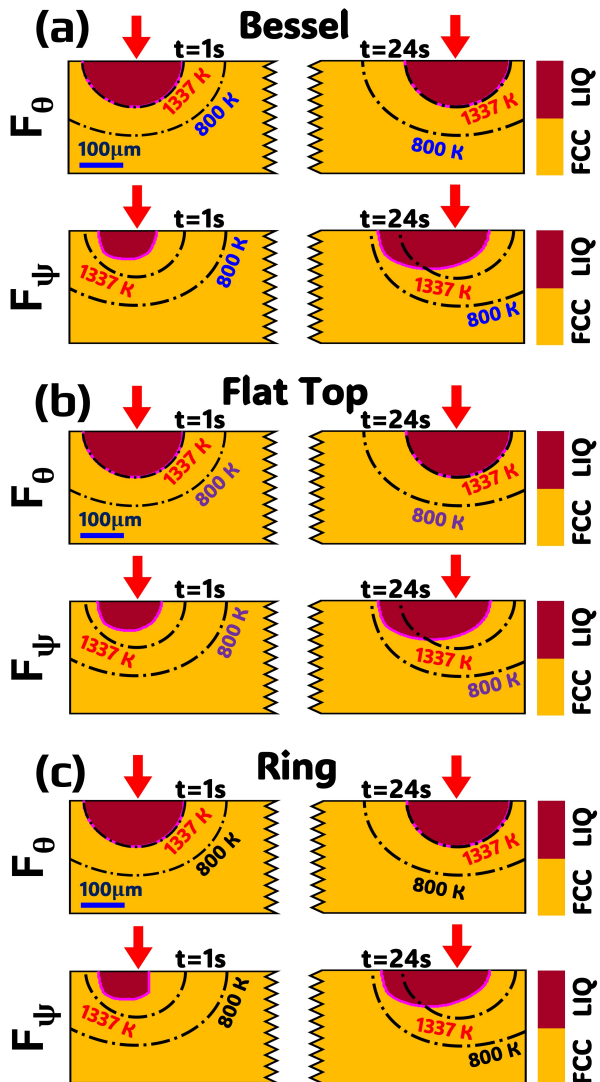


**Figure A3:** Visual illustration of laser induced phase evolution during the phase field simulation in unary Au system with different heat source profiles with different free energy expressions. (a) The four subplots depicts the growth of meltpool at time  $t=1\text{s}$  and  $t=24\text{s}$  under the Bessel beam with top row corresponding to fine-tuned free energy expression  $F_\theta$  and bottom row with  $F_\Psi$ . Similarly, in (b) the LIQUID phase status is presented for Flat-Top laser profile with  $F_\theta$  and  $F_\Psi$  as driving force for phase transformation in top and bottom row subplots. Finally (c) represents the meltpool phase growth similar to that of (a) and (b) but for the simulation with Ring laser beam under two free energy expressions. Although the different laser beam profile resulted in drastic temperature history and velocity profile inside the domain, the overall phase growth is in near similar fashion and is possible difficult to distinguish on a visual basis.